Summertime ozone formation in Xi'an and surrounding areas, China

T. Feng[1,2,3], N. Bei[1,2], R. Huang[2,4], J. Cao[2,3], Q. Zhang[5], W. Zhou[3], X. Tie[2,3], S. Liu[2,3], T. Zhang[2,3], X. Su[2,3], W. Lei[6], L. T. Molina[6], G. Li[2,3*]

(1) School of Human Settlements and Civil Engineering, Xi'an Jiaotong University, Xi'an, China
(2) Key Laboratory of Aerosol Chemistry and Physics, Institute of Earth Environment, Chinese Academy of Sciences, Xi'an, China
(3) State Key Laboratory of Loess and Quaternary Geology, Institute of Earth Environment, Chinese Academy of Sciences, Xi'an, China
(4) Laboratory of Atmospheric Chemistry, Paul Scherrer Institute (PSI), Villigen, Switzerland
(5) Department of Environmental Sciences and Engineering, Tsinghua University, Beijing, China
(6) Molina Center for Energy and the Environment, La Jolla, CA, USA

Abstract: In this study, the ozone (O_3) formation in China's northwest city of Xi'an and surrounding areas is investigated using the WRF-CHEM model during the period from August 22 to 24, 2013, corresponding to a heavy air pollution episode with high concentrations of O_3 and $PM_{2.5}$. The model generally performs well in simulating the surface temperature, relative humidity, wind speed and direction, near-surface O_3 and $PM_{2.5}$ mass concentrations, and aerosol constituents against measurements. High aerosol concentrations in Xi'an and surrounding areas significantly decrease the photolysis frequencies and can reduce O_3 concentrations by more than 50 μg m^{-3} (around 25 ppb) on average. Sensitivity studies show that the O_3 production regime in Xi'an and surrounding areas is complicated, varying from NO_x to VOC (Volatile Organic Compounds)-sensitive chemistry. The industrial emissions contribute the most to the O_3 concentrations compared to biogenic and other anthropogenic sources, but neither individual anthropogenic emission nor biogenic emission plays a dominant role in the O_3 formation. Under condition of high O_3 and $PM_{2.5}$ concentrations, a 50% reduction in all the anthropogenic emissions only decreases near-surface O_3 concentrations by about 14% during daytime. The complicated O_3 production regime and high aerosol levels pose a challenge for O_3 control strategies in Xi'an and surrounding areas. Further investigation on O_3 control strategies will need to be performed, taken into consideration the rapid changes in anthropogenic emissions that are not reflected in the current emission inventories, and the uncertainties in the meteorological field simulations.

Key words: ozone, $PM_{2.5}$, WRF-CHEM model, Xi'an

* Correspondence to: Guohui Li (ligh@ieecas.cn)

1. Introduction

Ozone (O_3) is a key species in the atmosphere due to its role in controlling the photochemistry in the stratosphere and troposphere (Seinfeld and Pandis, 2006) since O_3 and its photochemical derivative, OH, are the major oxidants for most reduced gases (Brasseur et al., 1999). Atmospheric O_3 also contributes to global climate change because of its absorption of the infrared radiation, constituting one of the important short-lived climate pollutants. Additionally, high levels of surface O_3 exert deleterious impacts on ecosystems and human health (Cao et al., 2012; Zhou et al., 2011) and O_3 is one of the criteria pollutants regulated by the environmental agencies in many countries, including US Environmental Protection Agency (US EPA) and the China's Ministry of Environmental Protection (China MEP).

Rapid industrialization and urbanization have caused widespread air pollution recently in China (e.g., De Smedt et al., 2010; Lu et al., 2011) and numerous studies have investigated the severe O_3 pollution, particularly in the Beijing-Tianjin-Hebei (BTH) region (e.g., Wang et al. 2006; Lin et al., 2008; Tang et al., 2009; Xu et al., 2011), Yangtze Delta (YRD) region (e.g., Geng et al., 2009, 2011; Tie et al., 2009, 2012), and Pearl River Delta (PRD) region (e.g., Zhang et al., 2008; Wang et al., 2009; Cheng et al., 2010; Wang et al., 2011; Li et al., 2013). For example, Wang et al. (2006) have observed strong O_3 production in urban plumes from Beijing with a maximum O_3 concentration of 286 ppb. Using a chemical transport model, Tie et al. (2009) have shown that unfavorable meteorological conditions cause high near-surface O_3 level exceeding 100 ppb in the Shanghai region. Wang et al. (2009) have reported increasing surface O_3 concentrations in the background atmosphere of Southern China from 1994 to 2007.

Xi'an, located in the Guanzhong basin, is the largest city in northwestern China with a population of more than 8 million. The basin is nestled between the Qinling Mountains in the south and the Loess Plateau in the north with a warm-humid climate. The unique topography

is not favorable for the dispersion of air pollutants (Figure 1a) and, with the fast growing industries and urban expansion, heavy air pollution often engulfs the basin (Cao et al., 2005; Shen et al., 2008, 2009). Shen et al. (2009) reported that the $PM_{2.5}$ (particulate matter with aerodynamic diameter less than 2.5 μm) mass concentrations in Xi'an exceed 350 μg m^{-3} during haze episodes, and the straw combustion in suburban area of Xi'an increases the $PM_{2.5}$ level to 400 μg m^{-3}. However, currently studies on surface O_3 measurements and formation mechanism in Xi'an are still limited. Wang et al. (2012) performed one-year surface O_3 measurement at an urban site in Xi'an in 2008 and observed high O_3 episodes with O_3 concentrations greater than 100 ppb in May and June; they found that these episodes are associated with biogenic emissions from Qinling Mountains. Considering the increasingly stringent air quality standards in China, studies are imperative to evaluate O_3 and other pollutants formation from both natural and anthropogenic emission sources to support the design and implementation of emission control strategies in the Guanzhong basin.

Since January 2013, China MEP has released the real-time hourly observations of chemical species at the national ambient monitoring stations, including O_3, NO_2, CO, SO_2, $PM_{2.5}$, and PM_{10} (particulate matter with aerodynamic diameter less than 10 μm). A total of thirteen national monitoring stations are distributed in the nine districts in Xi'an. In addition, continuous measurements of aerosol mass, chemical composition and optical properties have been conducted at the Institute of Earth Environment, Chinese Academy of Sciences (IEECAS) in Xi'an since 2003. All these measurements have provided an opportunity for investigating O_3 formation in Xi'an and surrounding areas. The purpose of the present study is to evaluate the O_3 formation from anthropogenic and natural sources and the challenges in designing O_3 control strategy due to the complicated nonlinear formation of O_3 and the aerosol impact on the photochemistry. The WRF-CHEM model and the model configuration

are described in Section 2. Results of the modeling experiments and comparisons are presented in Section 3, and the Conclusions are given in Section 4.

2. Model and Method

2.1 WRF-CHEM Model

In this study, a specific version of the WRF-CHEM model (Grell et al., 2005) is applied to verify the O_3 formation in Xi'an and surrounding areas, which was developed by Li et al. (2010; 2011a, b; 2012) at the Molina Center for Energy and the Environment, with a new flexible gas phase chemical module and the CMAQ (version 4.6) aerosol module developed by US EPA (Binkowski and Roselle, 2003). The wet deposition follows the method used in the CMAQ module and the dry deposition of chemical species is parameterized following Wesely (1989). The photolysis rates are calculated using the FTUV (Tie et al., 2003; Li et al., 2005) in which the impacts of aerosols and clouds on the photochemistry are considered (Li et al., 2011b).

We utilize ISORROPIA Version 1.7 (http://nenes.eas.gatech.edu/ISORROPIA/) to simulate the inorganic aerosols in the WRF-CHEM model. The inorganic aerosol module calculates the composition and phase state of an ammonium-sulfate-nitrate-chloride-sodium-calcium-potassium-magnesium-water inorganic aerosol in thermodynamic equilibrium with gas phase precursors. In the present study, the module is primarily used to predict the thermodynamic equilibrium between the ammonia-sulfate-nitrate-chloride-water aerosols and their gas phase precursors of H_2SO_4-HNO_3-NH_3-HCl-water vapor.

The secondary organic aerosol (SOA) formation is predicted using a non-traditional SOA module. The module includes the volatility basis-set (VBS) modeling method in which primary organic components are assumed to be semi-volatile and photochemically reactive and are distributed in logarithmically spaced volatility bins (Li et al., 2011a). Nine surrogate

species with saturation concentrations from 10^{-2} to 10^{6} μg m^{-3} at room temperature are used for the primary organic aerosol (POA) components following the approach of Shrivastava et al. (2008). Detailed description about the volatility basis-set approach can be found in Li et al. (2011a). The contributions of glyoxal and methylglyoxal to the SOA formation are also included in the SOA module. The SOA formation from glyoxal and methylglyoxal is parameterized as a first-order irreversible uptake by aerosol particles, with a reactive uptake coefficient of 3.7×10^{-3} for glyoxal and methylglyoxal (Zhao et al., 2006; Volkamer et al., 2007).

2.2 Model Configuration

A three-day episode from 22 to 24 August 2013 is selected for this study, representing a heavy air pollution event in Xi'an and surrounding areas with high levels of O_3 and $PM_{2.5}$. The WRF-CHEM model is configured with grid spacing of 3 km (201 × 201 grid points) centered at 34.25°N and 109°E (Figure 1a). Thirty-five vertical levels are used in a stretched vertical grid with spacing ranging from 50 m near the surface to 500 m at 2.5 km AGL and 1 km above 14 km. The modeling system employs the microphysics scheme of Lin et al. (1983); the MYJ TKE planetary boundary layer scheme and the MYJ surface layer scheme (Janjic, 2002); the Unified Noah land-surface model (Chen and Dudhia, 2000); the RRTM longwave radiation parameterization (Mlawer et al., 1997); and the Goddard shortwave module (Chou and Suarez, 1994). Meteorological initial and boundary conditions are obtained from NCEP 1°×1° reanalysis data. Chemical initial and boundary conditions are interpolated from MOZART 6-hour output (Horowitz et al., 2003). For the episode simulations, the spin-up time of the WRF-CHEM model is one day.

The SAPRC 99 chemical mechanism is utilized in the simulations. The anthropogenic emission inventory (EI) used in the present study is developed by Zhang et al. (2009), which includes contributions from agriculture, industry, power generation, residential and

transportation sources (Figure 2). High emissions of volatile organic compounds (VOCs) and nitrogen oxide (NO_x) are concentrated in Xi'an and surrounding areas. The primary organic aerosol emissions are redistributed following the study of Tsimpidi et al. (2010). Additionally, the biogenic emissions are calculated online with the WRF-CHEM model using the MEGAN model (Guenther et al., 2006).

2.3 Statistical Methods for Comparisons

In this study, the mean bias (*MB*), the root mean square error (*RMSE*), and the index of agreement (*IOA*) are used to evaluate the WRF-CHEM model simulations of meteorological parameters, gas-phase species, and aerosols.

$$MB = \frac{1}{N}\sum_{i=1}^{N}(P_i - O_i) \quad (1)$$

$$RMSE = \left[\frac{1}{N}\sum_{i=1}^{N}(P_i - O_i)^2\right]^{\frac{1}{2}} \quad (2)$$

$$IOA = 1 - \frac{\sum_{i=1}^{N}(P_i - O_i)^2}{\sum_{i=1}^{N}(|P_i - \bar{O}| + |O_i - \bar{O}|)^2} \quad (3)$$

where P_i and O_i are the simulated and observed variables, respectively. N is the total number of the predictions used for comparisons, and $\bar{O}$ denotes the average of the observation. *IOA* ranges from 0 to 1, with 1 indicating perfect agreement between model and observation.

2.4 Pollutants Measurements and Air Quality Standard in China

The real-time hourly measurements of O_3, NO_2, and $PM_{2.5}$ used in this study are released by China MEP and can be accessed from the website http://106.37.208.233:20035/. The historical profile of the observed ambient pollutants can be accessed at http://www.aqistudy.cn/. The O_3, NO_2, and $PM_{2.5}$ concentrations are measured by using Model 49*i* Ozone Analyzer, Model 42*i* (NO-NO_2-NO_x) Analyzer, and Model 5030 SHARP Monitor from Thermo Fisher Scientific, USA, respectively. All the instruments are maintained and routinely calibrated by China MEP to assure data quality.

The Chinese air quality standard released in 2012 is categorized into six levels based on the observed hourly and daily pollutants concentrations. During summertime, O_3 and $PM_{2.5}$ are the major atmospheric pollutants. A brief summary of the air quality standard based on the hourly O_3 and $PM_{2.5}$ concentrations is presented in Table 1.

3. Results and Discussion

3.0 Summertime Meteorological Fields and Air Quality in Xi'an

Figures 3a-d show the temporal variations of the temperature, relative humidity, wind speed and direction at Xianyang meteorological station (Figure 1c) during the summer of 2013. In general, the Guanzhong basin is hot and humid in the summer, with an average temperature of 26.7°C and relative humidity of 67.2% recorded at the Xianyang station. The winds are not strong in the basin; the average wind speed is around 3 m s^{-1} at the Xianyang station. During the simulation period, the observed average temperature, relative humidity, and wind speed at Xianyang station are 27.9°C, 63.4%, and 3.4 m s^{-1}, respectively, representing typical summertime meteorological conditions.

The profiles of summertime hourly O_3 and $PM_{2.5}$ concentrations averaged over 13 sites in Xi'an are also shown in Figures 3e and 3f, respectively, to provide an overview of the air quality in the summer of 2013. The observed average $PM_{2.5}$ and peak O_3 concentrations frequently exceed 75 and 160 μg m^{-3}, respectively, showing bad air quality in Xi'an. The simulation period corresponds to a heavy pollution episode with fairly high O_3 and $PM_{2.5}$ concentrations, which often occurs during summertime. Figure 4 further presents the monthly minimum, 5^{th} percentile, median, 95^{th} percentile, and maximum observations of near-surface O_3 concentrations in the afternoon averaged over 13 sites in Xi'an during the period from April 2013 to March 2014. The seasonal cycle of O_3 levels in Xi'an shows high summertime O_3 concentrations, which is consistent with that in North China Plain (Cooper et al., 2014). In

the study of Cooper et al. (2014), the midday O_3 mixing ratio in North China Plain peaks in June and then decreases in July and August due to the southerly monsoon flow. However, during the summer of 2013, the median O_3 concentration in the afternoon in Xi'an increases progressively from about 90 μg m^{-3} in June to 120 μg m^{-3} in August, with the maximum increasing from about 170 μg m^{-3} in June to 210 μg m^{-3} in August, which is possibly caused by the inland location of Xi'an with less monsoon precipitation during summertime.

Table 2 shows the comparison of summertime O_3 and $PM_{2.5}$ concentrations (averaged in the afternoon) in Xi'an to the main cities of BTH, YRD, and PRD in China during 2013. The O_3 and $PM_{2.5}$ concentrations in cities of BTH are much higher than those in Xi'an, showing the heavy air pollution in BTH. Due to the impact of frequent precipitation in South China, the $PM_{2.5}$ concentrations in the cities of YRD and PRD are lower than those in Xi'an, but the O_3 concentrations in Shanghai and Hangzhou are still higher than those in Xi'an. Generally, the air quality in Xi'an is better than that in the cities of BTH, but worse than that in Guangzhou of PRD.

3.1 Model Performance

For the discussion purpose, we have defined the reference simulation in which the emissions from various sources and aerosol effects on the photochemistry are included (hereafter referred to as REF), and results from the reference simulation are compared with the observations in Xi'an.

3.1.1 Meteorological Fields Simulations

Considering that the meteorological conditions play a crucial role in air pollution simulations (Bei et al., 2008, 2010, 2012), which determine the accumulation or dispersion of pollutants, verifications are first performed for the simulations of meteorological fields in Xi'an and surrounding areas. Figure 5 shows the temporal profiles of the simulated and observed surface temperature and relative humidity averaged over six meteorological

observation sites from August 22 to 24, 2013. The WRF-CHEM model reproduces successfully the temporal variations of the surface temperature during the three-day episode, but in general the model slightly underestimates the observations, particularly in the morning (Figure 5a). The *MB* and *RMSE* are -0.76 °C and 1.1 °C, respectively, and the *IOA* reaches 0.97, indicating good agreement of the surface temperature simulations with measurements (Table 3). The WRF-CHEM model generally tracks the temporal variations of the surface relative humidity well, with the *IOA* of 0.92 (Figure 5b). However, model underestimation of the observed surface relative humidity is obvious during midnight and morning. The *MB* and *RMSE* is -4.5% and 5.5% for the surface relative humidity simulations, respectively.

Figures 6 and 7 present the comparisons of simulated and observed wind speeds and directions at six meteorological observation sites from August 22 to 24, 2013, respectively. The model fails to yield the observed temporal variation of the wind speed at Xi'an site with the *IOA* of 0.26, and also significantly overestimates the observation with the *MB* of 1.7 m s^{-1} and *RMSE* of 2.1 m s^{-1}. In addition, fluctuating wind direction was observed at the Xi'an site; in contrast, the simulated winds was fixed in the northeast direction until the evening of August 23, and then changed to the southwest before noontime of August 24. As the Xi'an site is located in the urban center of Xi'an, it is surrounded by high buildings which significantly alter the airflow on the ground surface, causing light and disordered surface winds. Although the urban canopy model is utilized in the WRF-CHEM model simulations, the simulated surface winds are still biased considerably in the urban region due to the simplification of building distributions and heights and the inability of the model for micro-scale simulations (Chen et al., 2011; Lee et al., 2011). The simulated winds at Xi'an site are similar to those at Lintong, Xianyang, and Jinghe sites in the north of Xi'an, but in general, the wind simulations at these three sites are in good agreement with the observations, with the *IOA* of at least 0.61 for the wind speed, further suggesting the impacts of buildings in the

urban region on the wind simulations. The model performs well in predicting the wind speed and direction at Chang'an and Lantian sites in the south of Xi'an. It should be noted that the model considerably overestimates the observed wind speeds at all observations sites in the early morning of August 23 and also fails to track the variation of wind directions over the sites in the southern part of Xi'an, which causes the biased dispersion of the plume formed during daytime. In addition, the overestimation of the wind speed is also remarkable in the afternoon and evening of August 24, which evacuates the plume formed in the urban region more efficiently.

3.1.2 Gas-phase Species Simulations

The modeled O_3 and NO_2 mass concentrations are compared to the measurements at the ambient monitoring stations released by China MEP. Figure 8 shows the spatial distributions of calculated and observed near-surface O_3 concentrations at 08:00 and 15:00 Beijing Time (BJT) from August 22 to 24, 2013, along with the simulated wind fields. When the northeast wind is prevalent in the Guanzhong basin, due to the impact of the topography (Figure 1), the stagnant conditions are frequently formed in Xi'an and surrounding areas. At 08:00 BJT, the model underestimates the observed near-surface O_3 concentrations in the urban area of Xi'an, which is perhaps caused by the titration of NO emitted from traffic during rush hours. At 15:00 BJT, the calculated near-surface O_3 distributions are generally consistent with the observations at the ambient monitoring sites. On August 22, the northeast winds were strong and the stagnant region with high O_3 plume was located in the southwest of Xi'an and surrounding areas; the predicted O_3 concentrations are less than 160 μg m^{-3} in the urban area of Xi'an, in good agreement with the measurements. On August 23, the convergence in the urban area of Xi'an was favorable for the accumulation of O_3 precursors and the high O_3 plume was formed in the afternoon, with the O_3 concentration exceeding 200 μg m^{-3}. On August 24, the plume formed in the urban region of Xi'an was pushed to the south of Xi'an

and surrounding areas in the afternoon and the simulated O_3 concentrations were less than 200 μg m^{-3} in the urban area of Xi'an, generally consistent with the observations. In addition, the O_3 level in Xi'an and surrounding areas was also affected by the O_3 transport from its upwind region. It is worth noting that the model cannot replicate reasonably the spatial variation of the observed O_3 concentration at monitoring sites in the urban area of Xi'an. Although 3-km horizontal resolution is used in the study, it still cannot resolve adequately the spatial variation of O_3 concentrations over monitoring sites with the distance of less than 21 km (Skamarock, 2004). Unfortunately, the ambient monitoring sites in Xi'an are mainly concentrated in the urban area (around 20 km × 30 km), thus future model studies with higher horizontal resolution will be needed to improve the near-surface O_3 simulations under the present monitoring site distribution.

The simulated near-surface NO_2 distributions agree well with the observations at the ambient monitoring sites in the morning (Figures 9a, 9c, and 9e), with the highest NO_2 concentration in the urban center of Xi'an. In the afternoon, the model overestimates the observation in the urban center on August 23 while underestimates the observation on August 24.

Figure 10 displays the diurnal profiles of predicted and observed near-surface O_3 and NO_2 concentrations averaged over the ambient monitoring sites during the episode. The model tracks the temporal variations of surface O_3 concentrations well during daytime (Figure 10a), but the simulated O_3 concentrations deviates markedly from the observations in the early morning hours on August 23. Apparently, the plume with high O_3 concentrations formed in the southwest of Xi'an during daytime (Figure 8b) on August 22 was transported back to the urban area of Xi'an in the early morning on August 23, causing the observed high O_3 level. However, due to biases of the wind simulations in the early morning on August 23 (Figures 6 and 7), the plume formed from the previous day was not transported back to the

urban area of Xi'an, leading to the remarkable underestimation of the observed O_3 concentrations. The *MB*, *RMSE,* and *IOA* of the simulated O_3 concentration averaged over monitoring stations are -9.0 μg m^{-3}, 29 μg m^{-3}, and 0.91, respectively. Although the model reasonably well reproduces the variation of the observed NO_2 concentrations (Figure 10b), with *IOA* of 0.73, it often overestimates or underestimates the observation. Uncertainties in the simulated meteorological fields or the emission inventory might be responsible for the model biases in simulating NO_2 distributions and variations.

In summary, the calculated distribution and variation of near-surface O_3 and NO_2 concentrations are in good agreement with the corresponding observations, suggesting that the model simulates well the meteorological fields and the emission inventory used in the study is also reasonable.

3.1.3 Aerosol Simulations

Atmospheric particulate matter or aerosols scatter or absorb a fraction of solar radiation and increase or decrease the photolysis rates in the atmosphere, influencing the O_3 formation. Therefore, in order to reasonably verify the aerosol impact on photolysis and O_3 level, it is important to evaluate the simulated aerosol composition, variation and distribution using available measurements. Daily measurement of aerosol constituents is performed using the filter sample at IEECAS site, including sulfate, nitrate, ammonium, organic and elemental carbon. Figure 11a presents a scatterplot of the measured versus calculated daily mean concentration of aerosol constituents at IEECAS site from August 22 to 24, 2013. It should be noted that the simulated organic aerosol is compared with the filter measured organic carbon scaled by a factor of 2 (Carlton et al., 2010). The model performs well in simulating daily mean sulfate and organic aerosol concentrations. The model tends to overestimate the observed nitrate and ammonium concentration; this might be caused by the nitrate loss due to the evaporation from filters in the summer (Ianniello et al., 2011). The simulated daily mean

312 elemental carbon concentrations deviate from the measurements considerably on August 22
313 and 23, which is perhaps caused by the daily variations of elemental carbon emissions.
314 Comparison of the observed and modeled $PM_{2.5}$ mass composition averaged during the 3-day
315 episode is displayed in Figures 11b and 11c. Sulfate is the dominant constituent of the
316 observed $PM_{2.5}$ at IEECAS site, consisting of around 39% of the $PM_{2.5}$ mass, and the
317 simulated sulfate contribution to the $PM_{2.5}$ mass is about 35% on average, close to the
318 observation. The high sulfate concentrations come mainly from the SO_2 heterogeneous
319 reaction on aerosol surfaces under humid conditions (Wang et al., 2014). The measured and
320 modeled organic aerosols make up about 19% of the $PM_{2.5}$ mass at the IEECAS site, and
321 secondary organic aerosol contributes more than 50% of the modeled organic aerosol due to
322 the high atmospheric oxidation capacity in the summer. The modeled ammonium, nitrate, and
323 elemental carbon account for about 15%, 6.8%, and 3.1% of the $PM_{2.5}$ mass, respectively,
324 comparable to the observed 14%, 6.6%, and 3.6% at the IEECAS site.

325 Figure 12 shows the simulated geographic distributions of near-surface $PM_{2.5}$ mass
326 concentrations and the observations over the monitoring stations at 08:00 and 15:00 BJT
327 from August 22 to 24. On August 22, the convergence is formed in the north of Xi'an and
328 surrounding areas at 08:00 BJT, leading to the buildup of pollutants and high $PM_{2.5}$
329 concentrations. The simulated $PM_{2.5}$ concentrations are more than 75 $\mu g\ m^{-3}$ in the north of
330 Xi'an and surrounding areas, consistent with the measurements, but exceed 150 $\mu g\ m^{-3}$ in the
331 south where the stagnant conditions are formed and much higher than the observation. At
332 15:00 BJT, well organized northeast winds push the convergence zone to the southeast of
333 Xi'an and surrounding areas and the simulated $PM_{2.5}$ concentrations are less than 75 $\mu g\ m^{-3}$,
334 in good agreement with the measurements. On August 23, the convergence is withheld in the
335 urban area of Xi'an, causing heavy $PM_{2.5}$ pollution. The calculated $PM_{2.5}$ concentration is
336 more than 115 $\mu g\ m^{-3}$ at 08:00 and 15:00 BJT, comparable to the measurements. The

observed and simulated $PM_{2.5}$ patterns on August 23 are similar to those on August 23, but the $PM_{2.5}$ concentrations on August 24 are enhanced. For example, the observed and simulated $PM_{2.5}$ concentrations over all monitoring stations exceed 150 μg m^{-3} at 08:00 BJT. In addition, at 15:00 BJT, due to the overestimation of the wind speed (Figure 6), the convergence zone is pushed to the south of Xi'an and surrounding areas, causing the underestimation of $PM_{2.5}$ concentration in the north. The model reproduces the observed diurnal profile of the $PM_{2.5}$ concentration averaged over the monitoring stations during the episode (Figure 13), with *MB* of -1.4 μg m^{-3}, *RMSE* of 21 μg m^{-3}, and *IOA* of 0.92. Apparently, the convergence zone location, which is determined by the meteorological fields, significantly influences the $PM_{2.5}$ simulations. When the simulated convergence zone is formed in the south of Xi'an and surrounding areas on the morning of August 22, the model considerably overestimates the observed $PM_{2.5}$ concentration. However, when the simulated winds are too strong and the convergence zone is pushed to the south of Xi'an and surrounding areas on August 23, the model notably underestimates the observations.

The simulated column-integrated aerosol optical depth (AOD) and single scattering albedo (SSA) are verified using the available measurements from the surface site and satellite. The simulated aerosol optical properties are calculated using the method developed by Li et al. (2011b). Figures 14a and 14b show the comparison of simulated column-integrated AOD and aerosol SSA at 440 nm with measurements at IEECAS site, respectively, which is retrieved from the observations of a sun-sky radiometer (Su et al., 2014). The simulated AOD on August 22 is comparable to the measurements at IEECAS site, but the WRF-CHEM model overestimates the observation in the morning due to the overestimation of $PM_{2.5}$ concentrations. The simulated SSA on August 22 ranges from 0.92 to 0.95, close to the measurement. However, on August 23, the retrieved AOD and SSA exceed 3.0 and 0.95, respectively, higher than the corresponding simulations. The underestimation of the

simulated AOD and aerosol SSA could be attributed to the underestimation of the relative humidity, not limited to the ground surface as shown in Figure 5. The distribution of the calculated AOD at 550 nm from MODIS (Moderate Resolution Imaging Spectroradiometer) aerosol level-2 product at 5×5 1-km pixel resolution is also compared with the model results (Figures 14c and 14d). The simulated AOD pattern on August 22 is agrees well with the measurements, except over the Qinling Mountains where the convection is active. The model underestimates the observed AOD in the north of Xi'an on August 23, which is likely caused by the bias of the simulated relative humidity. Apparently, the AOD at 550 nm in Xi'an and surrounding areas is high, exceeding 0.8 on August 22 and 1.0 on August 23.

3.2 Sensitivity Studies

3.2.1 Effects of Aerosol on the O_3 Formation

O_3 formation in the atmosphere is a complicated photochemical process, which is determined by its precursors from various sources and transformation in the presence of sunlight. High AOD in Xi'an and surrounding areas efficiently scatter or absorb sunlight to decrease the photolysis frequencies in the planetary boundary layer (PBL) and further the O_3 formation. High O_3 levels enhance atmospheric oxidation capability and the secondary aerosol formation, increasing the aerosol concentration in the atmosphere, but conversely, high aerosol levels decrease the photolysis frequencies and suppress the O_3 formation in the PBL. The interactions of O_3 with aerosols complicate the design of O_3 control strategies.

The aerosol effect on O_3 formation in Xi'an and surrounding areas is examined by the sensitivity study without aerosol effects on the photolysis compared to the reference simulation (hereafter we define the sensitivity simulation as SEN). Figures 15a and 15b present the diurnal profiles of the change of the NO_2 photolysis frequency ($J[NO_2]$) and O_3 concentration averaged in Xi'an and surrounding areas due to aerosol effects from August 22 to 24, respectively. Aerosols significantly decrease $J[NO_2]$ by 30-70% (defined as (REF-

SEN)/SEN) in the early morning and late afternoon hours when the solar zenith angle is large, showing the impact of long aerosol optical path for incoming radiation. Due to the high aerosol level, the aerosol effect on $J[NO_2]$ is still substantial during noontime, decreasing $J[NO_2]$ by over 20% on August 23 and 24 when the plume is stagnant in the urban region of Xi'an. The aerosol effect on the photolysis frequency in this study is larger than those reported in other studies (e.g., Jacobson, 1998; Li et al., 2005, 2011b). The aerosol impact on O_3 formation is most significant during the late morning and early afternoon (Figure 15b). On average, in Xi'an and surrounding areas, the reduction in O_3 concentration (defined as (REF-SEN)) due to the aerosol effect on photolysis is less than 20 μg m^{-3} on August 22, but more than 30 μg m^{-3} during noontime on August 23 and over 50 μg m^{-3} in the late morning on August 24. The aerosol effect on O_3 formation in this study is comparable to those reported by Castro et al. (2001) in Mexico City. It should be noted that the impact of photolysis on O_3 level varies depending on the ratio of VOCs to NO_x (Stockwell and Goliff, 2004). The important aerosol effects on O_3 formation may pose a dilemma for O_3 control strategies. If O_3 concentrations are decreased by reducing its precursor's emissions, the aerosol level will also decrease due to direct and indirect contributions from the emission control, which compensates the O_3 reduction by enhancing the photolysis frequency.

3.2.2 O_3 Response to Emission Changes

In the urban area, when the meteorological conditions are favorable for the accumulation of pollutants in the PBL, the O_3 precursors of anthropogenically or naturally emitted VOCs and NO_x, react chemically in the presence of sunlight, leading to high O_3 level. In order to devise effective O_3 control strategy, it is important to investigate the regime of O_3 production. The regime of O_3 production in Xi'an and surrounding areas is examined using sensitivity studies by reducing anthropogenic VOCs (AVOCs) or NO_x emissions by 50% in the WRF-CHEM simulations. Figure 16 compares the near-surface O_3 concentrations

412 averaged in the urban area of Xi'an in the reference simulation to the two sensitivity studies
413 in which AVOCs and NO_x are decreased by 50%, respectively. A 50% reduction in AVOCs
414 decreases the O_3 concentration averaged in Xi'an surrounding areas consistently during the
415 episode, particularly during peak time (defined as 1400-1600 BJT hereafter). A 50%
416 reduction in NO_x enhances the O_3 level in the morning due to the decrease of NO emission;
417 but in the afternoon, it decreases the O_3 level, similar to the effect from a 50% reduction in
418 AVOCs, leading to a complicated O_3 production regime.

419 Figure 17a shows the 3-day average near-surface O_3 change during peak time with a 50%
420 reduction in NO_x emissions (defined as O_3(SEN) – O_3(REF)). In Xi'an and surrounding areas,
421 except the urban center, the simulated average O_3 concentrations are decreased by about 10-
422 40 μg m^{-3} due to a 50% reduction in NO_x. In the urban center, the O_3 concentrations are
423 enhanced only with very high NO_x emissions, but less than 10 μg m^{-3}. A 50% reduction in
424 AVOCs emissions consistently reduces the O_3 concentration in Xi'an and surrounding areas
425 by up to 40 μg m^{-3} (Figure 17b). The response of O_3 change to a 50% reduction in NO_x or
426 AVOCs emissions cannot clearly indicate the O_3 production regime in Xi'an and surrounding
427 areas.

428 Sillman (1995) proposed that the ratio of the production rates of hydrogen peroxide and
429 nitric acid ($P(H_2O_2)/P(HNO_3)$) can be used to investigate the sensitivity of ozone formation to
430 the precursors. If the ratio of $P(H_2O_2)/P(HNO_3)$ is less than 0.3, the O_3 production regime is
431 VOC-sensitive. If the ratio exceeds 0.5, the regime is NO_x-sensitive. The ratio ranging from
432 0.3 to 0.5 indicates the transition from NO_x to VOC-sensitive regime. Figure 17c displays the
433 distribution of the 3-day average $P(H_2O_2)/P(HNO_3)$ during the O_3 peak time. In Xi'an and
434 surrounding areas, the $P(H_2O_2)/P(HNO_3)$ ratio varies from 0.2 to 1.0, suggesting that the O_3
435 production regime is very complicated. In the south of Xi'an and surrounding areas, the O_3
436 production regime lies in the transition from NO_x to VOC-sensitive chemistry. The analyses

using $P(H_2O_2)/P(HNO_3)$ indicator and the results obtained from the two sensitivity studies suggested that it is not straightforward to devise effective O_3 control strategies for Xi'an and surrounding areas.

3.2.3 O_3 Contribution from Natural and Anthropogenic Sources

Biogenic emissions provide natural O_3 precursors and numerous studies have shown that biogenic VOCs play an important role in ground-level O_3 formation in the urban areas (e.g., Solmon et al., 2004; Li et al., 2006), thus complicating O_3 control strategy. A sensitivity study without biogenic emissions is conducted and compared with the reference simulation to evaluate the contribution of biogenic emissions to ozone production. During noontime, biogenic emissions contribute about 0.3 ppb isoprene averaged in Xi'an and surrounding areas, and the O_3 contribution from biogenic emissions is around 10 μg m^{-3} (Figure 18). Large amounts of biogenic emissions are released over the Qinling Mountains on the south of Xi'an, and can be transported to the urban area under favorable meteorological conditions, enhancing O_3 formation. However, the northeast wind is prevalent in the Guanzhong basin during daytime, which is not favorable for the transport of biogenic emissions from the Qinling Mountains. Although the O_3 level enhanced by biogenic emissions is not significant in Xi'an and surrounding areas, the high reactivity of biogenic VOCs, such as isoprene and monoterpenes, will play an increasing important role in O_3 formation when the anthropogenic VOCs are decreased as a result of O_3 control measures.

We have further used the sensitivity studies to evaluate contribution of anthropogenic emissions from indutrial, residential and transportation sources, respectively, to O_3 production. The industrial emissions contribute more than 70% of the anthropogenic VOCs, and play the most important role in the O_3 formation in Xi'an and surrounding areas during daytime, compared to residential and transportation emissions. On average, the near-surface O_3 contribution from industrial emissions is about 10-30 μg m^3 in the afternoon and exceeds

20 μg m^{-3} during O_3 peak time (Figure 19b). Transportation emissions contribute about 10 to 20 μg m^{-3} ozone in the afternoon, while residential emissions contribute less than 10 μg m^{-3} O_3.

Sensitivity studies have shown that there is no single anthropogenic ozone precursor emission source that dominates the O_3 level in Xi'an and surrounding areas. The simulation without the most important industrial source still predicts high near-surface O_3 concentrations in Xi'an and surrounding areas (Figure 19a). The O_3 production regime in Xi'an and surrounding areas varies from NO_x to VOC-sensitive chemistry, constituting one of the possible reasons for the insensitivity of O_3 concentration to the emission change. Additionally, in case of high aerosol levels, aerosol effects on photolysis also compensate the O_3 decrease through enhancing photolysis frequencies due to decrease of aerosol concentrations caused by the emission reduction. Although biogenic emission does not play a major role in the O_3 formation in Xi'an and surrounding areas, it provides reactive VOCs precursor for O_3 formation. Therefore, under the situation with high O_3 and $PM_{2.5}$ in Xi'an and surrounding areas, decreasing emissions from various anthropogenic sources alone cannot efficiently mitigate the O_3 pollution. Sensitivity studies have been performed to further demonstrate the difficulties in devising O_3 control strategies through decreasing anthropogenic emissions from industry, residential, transportation, and all the anthropogenic sources by 50%, respectively in the WRF-CHEM simulations. A 50% reduction in industrial emissions only resulted in less than 7% decrease of O_3 concentrations in Xi'an and surrounding areas (Figure 20). Even if all the anthropogenic emissions are reduced by 50%, the decrease in O_3 concentrations is not more than 14%.

4. Summary and Conclusions

In this study, a 3-day episode with high O_3 and $PM_{2.5}$ concentrations from August 22 to

24, 2013, is simulated using the WRF-CHEM model to evaluate the O_3 formation in Xi'an and surrounding areas. The WRF-CHEM model generally performs well in simulating the surface temperature and relative humidity compared to the observations and also reasonably reproduces the observed temporal variations of the surface wind speed and direction. The convergence formed in Xi'an and surrounding areas is favorable for the accumulation of pollutants, leading to high concentrations of O_3 and $PM_{2.5}$. In general, the calculated spatial patterns and temporal variations of near-surface O_3 and $PM_{2.5}$ are consistent with the measurement at the ambient monitoring stations. The simulated daily mass concentrations of aerosol constituents, including sulfate, nitrate, ammonium, elemental and organic carbon, are also in good agreement with the filter measurements. The simulated column-integrated AOD at 550 nm and SSA at 440 nm are compared to the available measurements from the surface site and satellite. The calculated AOD and SSA agree well with the measurements on August 22, but the AOD and SSA simulations are biased considerably on August 23, which is perhaps caused by underestimation of the relative humidity.

High aerosol levels significantly decrease the photolysis frequencies in Xi'an and surrounding areas. On average, the $J[NO_2]$ at the ground surface is decreased by 30-70% in the early morning and late afternoon when the solar zenith angle is large, and even around noontime, the decrease of $J[NO_2]$ is still significant, exceeding 20% on August 23 and 24. The aerosol effect on photolysis remarkably decreases the O_3 formation in the late morning and early afternoon, with the O_3 reduction of more than 50 μg m^{-3} on average in Xi'an and surrounding areas. The significant aerosol effects on O_3 formation complicate the design of O_3 control strategies. If the O_3 mitigation causes the reduction of aerosols directly and indirectly, the enhanced photolysis due to the aerosol decrease compensates the O_3 reduction.

Sensitivity studies demonstrate that the O_3 production regime in Xi'an and surrounding areas varies from NO_x to VOC-sensitive chemistry, constituting a dilemma for O_3 control

strategies. Studies in North China show that the BTH area is under a VOC-sensitive regime (Wang et al, 2006; Tang et al., 2012). Xue et al. (2014) also reports that O_3 production is VOC-limited in both Shanghai and Guangzhou, but NO_x-limited in Lanzhou. The industrial emissions contribute the most to the O_3 concentrations in Xi'an and surrounding areas, but neither individual anthropogenic emission nor biogenic emissions play a dominant role in the O_3 formation. Under the situation with high O_3 and $PM_{2.5}$ concentrations in Xi'an and surrounding areas, mitigation of O_3 pollutions is challenging through decreasing emissions from various anthropogenic sources. A 50% reduction in all the anthropogenic emissions only decreases the near-surface O_3 level by less than 14% on average in Xi'an and surrounding areas.

Xi'an and surrounding areas, with more than 10 million population, are a representative region in the northwest of China, experiencing rapid industrialization and urbanization in recent years. Heavy haze or photochemical smog events frequently engulf the region, substantially impairing visibility and potentially causing severe health effects. Although the dispersion conditions have improved during summertime, the occurrence of heavy pollution events with both high $PM_{2.5}$ and O_3 levels is frequent in the region, exceeding China air quality standards (Table 1). We have defined two exceedance levels: Level I with hourly $PM_{2.5}$ and O_3 concentrations exceeding 35 and 160 μg m^{-3}, respectively, and Level II with hourly $PM_{2.5}$ and O_3 concentrations exceeding 75 and 200 μg m^{-3}, respectively. We have further analyzed the real-time hourly observations of $PM_{2.5}$ and O_3 concentrations in the afternoon in mega-cities or urban complexes of the northern part of China, to explore the occurrence days of the defined exceedance levels during 2013 summertime (Table 4). As shown in Table 4, in Tianjin, Shijiazhuang, and Ji'nan, the number of days of exceedance level II is more than 40, that is, haze and photochemical smog events hit the three cities simultaneously at least 40 days in the afternoon during 2013 summertime. Thus, the model

results in the present study, from an episode with high concentrations of O_3 and $PM_{2.5}$ in Xi'an and surrounding areas, can potentially provide beneficial support for the design and implementation of emission control strategies in those cities in North China. The occurrence of high O_3 levels with high $PM_{2.5}$ concentrations constitutes a dilemma for the design of O_3 control strategies. If the O_3 mitigation approach decreases aerosols in the atmosphere directly or indirectly, the enhanced photolysis caused by aerosol reduction would compensate the O_3 loss. If the $PM_{2.5}$ control strategy is implemented only, the O_3 pollution will be deteriorated. Since the release of "Atmospheric Pollution Prevention and Control Action Plan" in 2013 (http://www.gov.cn/zwgk/2013-09/12/content_2486773.htm), the stringent $PM_{2.5}$ control strategy has been implemented in China. The summertime $PM_{2.5}$ concentration in the afternoon in Xi'an has decreased from 48.5 μg m^{-3} in 2013 to 38.8 μg m^{-3} in 2014; however, the O_3 concentration has increased from 104.6 μg m^{-3} in 2013 to 114.7 μg m^{-3} in 2014. The same trend is also found in the cities of BTH: the $PM_{2.5}$ concentration has decreased from 71.5 μg m^{-3} in 2013 to 57.4 μg m^{-3} in 2014, while the O_3 concentration has increased from 125.8 μg m^{-3} in 2013 to 139.1 μg m^{-3} in 2014. Therefore, the decrease of the $PM_{2.5}$ level might enhance O_3 production, which is consistent with the results in the present study.

It is worth noting that, although the WRF-CHEM model generally performs well in the simulations of the gas-phase species and aerosols compared to measurements, it still sometimes underestimates or overestimates the observations. One of the possible reasons for the discrepancies between simulations and observations is the uncertainty of the emission inventory, which has undergone noticeable changes due to rapid urbanization and industrialization and implementation of air pollution control strategies in the Guanzhong basin since the base year (2010) when the emission inventory was developed; thus the emission inventory will need updating in future studies. The model results are also sensitive to the meteorological field uncertainty, e.g., the biases of modeled wind fields significantly

impact the simulations of the variation and pattern of the gas-phase species and aerosols in the early morning on August 23 and in the afternoon on August 24. Studies need to be conducted to further improve the meteorological field simulations in Xi'an and surrounding areas for the assessment of the O_3 formation.

Data availability: The real-time O_3, NO_2 and $PM_{2.5}$ are accessible for the public on the website http://106.37.208.233:20035/. One can also access the historic profile of observed ambient pollutants through visiting http://www.aqistudy.cn/.

Acknowledgements. This work was supported by the National Natural Science Foundation of China (no. 41275153) and the "Hundred Talents Program" of the Chinese Academy of Sciences. Naifang Bei is supported by the National Natural Science Foundation of China (no. 41275101).

577 **Reference:**

578 Bei, N., de Foy, B., Lei, W., Zavala, M., and Molina, L.T.: Using 3DVAR data assimilation
579 system to improve ozone simulations in the Mexico City basin, Atmos. Chem. Phys., 8,
580 7353–7366, 2008.

581 Bei, N., Lei, W., Zavala, M., and Molina, L.T.: Ozone predictabilities due to meteorological
582 uncertainties in Mexico City Basin using ensemble forecasts, Atmos. Chem. Phys., 10,
583 6295–6309, 2010.

584 Bei, N., Li, G., and Molina, L.T.: Uncertainties in SOA simulations due to meteorological
585 uncertainties in Mexico City during MILAGRO-2006 field campaign, Atmos. Chem.
586 Phys., 12, 11295–11308, 2012.

587 Binkowski, F. S. and Roselle, S. J.: Models-3 Community Multiscale Air Quality (CMAQ)
588 model aerosol component 1. Model description, J. Geophys. Res., 108(D6), 4183–18,
589 doi:10.1029/2001JD001409, 2003.

590 Brasseur, G. P., Orlando, J. J., and Tyndall, G. S.: Atmospheric chemistry and global change,
591 Oxford University Press, Cambridge, USA, 654 pp, 1999.

592 Cao, J. J., Wu, F., Chow, J. C., Lee, S. C., Li, Y., Chen, S. W., An, Z. S., Fung, K. K.,
593 Watson, J. G., Zhu, C. S., and Liu, S. X.: Characterization and source apportionment of
594 atmospheric organic and elemental carbon during fall and winter of 2003 in Xi'an, China,
595 Atmos. Chem. Phys, 5, 3127–3137, 2005.

596 Cao, J., Xu, H., Xu, Q., Chen, B., and Kan, H.: Fine particulate matter constituents and
597 cardiopulmonary mortality in a heavily polluted Chinese city, Environ. Health Persp., 120,
598 373–378, 2012.

599 Castro, T., Madronich, S., Rivale, S., Muhlia, A., and Mar B.: The influence of aerosols on
600 photochemical smog in Mexico City, Atmos. Environ., 35, 1765–1772, 2001.

601 Chen, F., and Dudhia, J.: Coupling an advanced land-surface/hydrology model with the Penn
602 State/NCARMM5modelingsystem. Part I: Model description and implementation, Mon.
603 Wea. Rev., 129, 569–585, 2001.

604 Chen, F., Kusaka, H., Bornstein, R., Ching, J., Grimmond, C. S. B., Grossman-Clarke, S.,
605 Loridan, T., Manning, K. W., Martilli, A., Miao, S., Sailor, D., Salamanca, F. P., Taha, H.,
606 Tewari, M., Wang, X., Wyszogrodzki, A. A. and Zhang, C.: The integrated WRF/urban
607 modelling system: development, evaluation, and applications to urban environmental
608 problems, edited by M. Roth, R. Emmanuel, T. Ichinose, and J. Salmond, Int. J. Climatol.,
609 31(2), 273–288, doi:10.1002/joc.2158, 2011.

610 Cheng, H. R., Guo, H., Saunders, S. M., Lam, S. H. M., Jiang, F., Wang, X. M., Simpson, I.
611 J., Blake, D. R., Louie, P. K. K., and Wang, T. J.: Assessing photochemical ozone
612 formation in the Pearl River Delta with a photochemical trajectory model, Atmos.
613 Environ., 44, 4199–4208, 2010.

614 Chou, M.-D., and Suarez, M. J.: An efficient thermal infrared radiation parameterization for
615 use in general circulation models. NASA Tech. Memo. 104606, 3, 85 pp., 1994.

616 Cooper, O. R., Parrish, D. D., Ziemke, J., Balashov, N. V., Cupeiro, M., Galbally, I. E., Gilge,
617 S., Horowitz, L., Jensen, N. R., Lamarque, J. F., Naik, V., Oltmans, S. J., Schwab, J.,
618 Shindell, D. T., Thompson, A. M., Thouret, V., Wang, Y. and Zbinden, R. M.: Global
619 distribution and trends of tropospheric ozone: An observation-based review, Elem. Sci.
620 Anth., 2(1), 000029–28, doi:10.12952/journal.elementa.000029, 2014.

De Smedt, I., T. Stavrakou, J. F. Muller, et al.: Trend detection in satellite observations of formaldehyde tropospheric columns, Geophys. Res. Lett., 37, L18808, doi:10.1029/2010GL044245, 2010.

Geng, F. H., Qiang, Z., Tie, X., Huang, M., Ma, X., Deng, Z., Quan, J., and Zhao, C.: Aircraft measurements of O_3, NO_x, CO, VOCs, and SO_2 in the Yangtze River Delta region, Atmos. Environ., 43, 584–593, 2009.

Geng, F., Tie, X., Guenther, A., Li, G., Cao, J., and Harley, P.: Effect of isoprene emissions from major forests on ozone formation in the city of Shanghai, China, Atmos. Chem. Phys., 11, 10449–10459, 2011.

Guenther, A., Karl, T., Harley, P., Wiedinmyer, C., Palmer, P.I., and Geron, C.: Estimates of global terrestrial isoprene emissions using MEGAN (Model of Emissions of Gases and Aerosols from Nature), Atmos. Chem. Phys., 6, 3181–3210, 2006.

Grell, G.A., Peckham, S.E., Schmitz, R., McKeen, S.A., Wilczak, J., and Eder, B.: Fully coupled "online" chemistry within the WRF model, Atmos. Environ., 39, 6957–6975, 2005.

Horowitz, L. W., et al.: A global simulation of tropospheric ozone and related tracers: Description and evaluation of MOZART, version 2, J. Geophys. Res., 108(D24), 4784, doi:10.1029/2002JD002853, 2003.

Jacobson, M. Z.: Studying the effects of aerosols on vertical photolysis rate coefficient and temperature profiles over an urban airshed, J. Geophys. Res., 103, 10,593–10,604, 1998.

Janjic, Z. I., 2002: Nonsingular implementation of the Mellor-Yamada Level 2.5 Scheme in the NCEP Meso model, NCEP Office Note No. 437, 61 pp., 2002.

Lee, S. H., Kim, S. W., Angevine, W. M., Bianco, L., McKeen, S. A., Senff, C. J., Trainer, M., Tucker, S. C. and Zamora, R. J.: Evaluation of urban surface parameterizations in the WRF model using measurements during the Texas Air Quality Study 2006 field campaign, Atmos. Chem. Phys., 11(5), 2127–2143, doi:10.5194/acp-11-2127-2011, 2011.

Li, G., Zhang, R., Fan, J., and Tie, X.: Impacts of black carbon aerosol on photolysis and ozone, J. Geophys. Res., 110, D23206, doi:10.1029/2005JD005898, 2005.

Li, G., Zhang, R., Fan, J., and Tie, X.: Impacts of biogenic emissions on photochemical ozone production in Houston, Texas, J. Geophys. Res., 112, D10309, doi:10.1029/2006JD007924, 2007.

Li, G., Lei, W., Zavala, M., Volkamer, R., Dusanter, S., Stevens, P., and Molina, L.T.: Impacts of HONO sources on the photochemistry in Mexico City during the MCMA-2006/MILAGO Campaign, Atmos. Chem. Phys., 10, 6551–6567, 2010.

Li, G., Zavala, M., Lei, W., Tsimpidi, A.P., Karydis, V.A., Pandis, S.N., Canagaratna, M.R., and Molina, L.T.: Simulations of organic aerosol concentrations in Mexico City using the WRF-CHEM model during the MCMA-2006/MILAGRO campaign, Atmos. Chem. Phys., 11, 3789–3809, 2011a.

Li, G., Bei, N., Tie, X., and Molina, L.T.: Aerosol effects on the photochemistry in Mexico City during MCMA-2006/MILAGRO campaign, Atmos. Chem. Phys., 11, 5169–5182, 2011b.

Li, G., Lei, W., Bei, N., and Molina, L.T.: Contribution of garbage burning to chloride and $PM_{2.5}$ in Mexico City, Atmos. Chem. Phys., 12, 8751–8761, 2012.

Lin Y.-L., Farley, R. D., and Orville, H. D.:, Bulk parameterization of the snow field in a cloud model, J. Appl. Meteorol., 22, 1065–1092, 1983.

Lin, W. L., Xu, X. B., Zhang, X. C., and Tang, J.: Contributions of pollutants from North China Plain to surface ozone at the Shangdianzi GAW Station, Atmos. Chem. Phys., 8, 5889–5898, 2008.

Lu, Z., Zhang, Q., and Streets, D. G.: Sulfur dioxide and primary carbonaceous aerosol emissions in China and India, 1996–2010, Atmos. Chem. Phys., 11, 9839–9864, 2011.

Mlawer, E. J., Taubman, S. J., Brown, P. D., Iacono, M. J., and Clough, S. A.: Radiative transfer for inhomogeneous atmosphere: RRTM, a validated correlated-k model for the long-wave J. Geophys. Res., 102, D14, 16663–16682, 1997.

Seinfeld, J. H. and Pandis, S. N.: Atmospheric chemistry and physics: from air pollution to climate Change, 2nd Edition, John Wiley & Sons, Inc., New York, USA, 1326 pp., 2006.

Shen, Z. X., Arimoto, R., Okuda, T., Cao, J. J., Zhang, R. J., Li, X. X., Du, N., Nakao, S., Tanaka, S.: Seasonal variations and evidence for the effectiveness of pollution controls on water-soluble inorganic species in TSP and PM2.5 from Xi'an, China, J. Air Waste Manage, 58, 1560–1570, 2008.

Shen, Z., Cao, J., Arimoto, R., Han, Z., Zhang, R., Han, Y., Liu, S., Okuda, T., Nakao, S., and Tanaka, S.: Ionic composition of TSP and PM2.5 during dust storms and air pollution episodes at Xi'an, China, Atmos. Environ., 43, 2911–2918, 2009.

Shrivastava, M. K., Lane, T. E., Donahue, N. M., Pandis, S. N., and Robinson, A. L.: Effects of gas-particle partitioning and aging of primary emissions on urban and regional organic aerosol concentrations, J. Geophys. Res., 113, D18301, doi:10.1029/2007JD009735, 2008.

Sillman, S., The use of NO_y, H_2O_2 and HNO_3 as indicators for O_3-NO_x-VOC sensitivity in urban locations, J. Geophys. Res., 100, 14,175–14,188, 1995.

Skamarock, W. C.: Evaluating Mesoscale NWP models using kinetic energy spectra, Mon. Wea. Rev., 132, 3019–3032, 2004.

Solmon, F., Sarrat, C., Serça, D., Tulet, P. and Rosset, R.: Isoprene and monoterpenes biogenic emissions in France: modeling and impact during a regional pollution episode, Atmos. Environ., 38(23), 3853–3865, doi:10.1016/j.atmosenv.2004.03.054, 2004.

Stockwell, W. R., and Goliff, W. S.: Measurement of actinic flux and the calculation of photolysis rate parameters for the Central California Ozone Study, Atmos. Environ., 38, 5169–5177, 2004.

Su, X., Cao, J., Li, Z., Lin, M., and Wang, G.: Column-integrated aerosol optical properties during summer and autumn of 2012 in Xi'an, China, Aerosol Air Qual. Res., 14, 850–861, 10.4209/aaqr.2013.03.0093, 2014.

Tang, G., Li, X., Wang, Y., Xin, J., and Ren, X. C.: Surface ozone trend details and interpretations in Beijing, 2001–2006, Atmos. Chem. Phys., 9, 8813–8823, 2009.

Tang, G., Wang, Y., Li, X., Ji, D., Hsu, S. and Gao, X.: Spatial-temporal variations in surface ozone in Northern China as observed during 2009–2010 and possible implications for future air quality control strategies, Atmos. Chem. Phys., 12(5), 2757–2776, doi:10.5194/acp-12-2757-2012, 2012.

Tie, X., Geng, F. H., Peng, L., Gao, W., and Zhao, C. S.: Measurement and modeling of O_3 variability in Shanghai, China; Application of the WRF-CHEM model, Atmos. Environ., 43, 4289–4302, 2009.

Tie, X., Geng, F., Guenther, A., Cao, J., Greenberg, J., Zhang, R., Apel, E., Li, G., Weinheimer, A., Chen, J., and Cai, C.: Megacity impacts on regional ozone formation: observations and WRF-CHEM modeling for the MIRAGE-Shanghai field campaign, Atmos. Chem. Phys., 13, 5655–5669, 2013.

Tie, X., Madronich, S., Walters, S., Zhang, R., Rasch, P., and Collins, W.: Effect of clouds on photolysis and oxidants in the troposphere, J. Geophys. Res., 108(D20), 4642, doi:10.1029/2003JD003659, 2003.

Tsimpidi, A. P., Karydis, V. A., Pandis, S. N., Zavala, M., Lei, W., and Molina, L. T.: Evaluation of the Volatility Basis-Set Approach for Modeling Primary and Secondary Organic Aerosol in the Mexico City Metropolitan Area, Atmos. Chem. Phys., 10, 525–546, 2010.

Volkamer, R., San Martini, F., Molina, L. T., et al.: A Missing Sink for Gas-Phase Glyoxal in Mexico City: Formation of Secondary Organic Aerosol, Geophys. Res. Lett., 34, L19807, doi:10.1029/2007GL030752, 2007.

Wang, T., Ding, A., Gao, J., and Wu, W. S.:, Strong ozone production in urban plumes from Beijing, China, Geophys. Res. Lett., 33, L21806, doi:10.1029/2006GL027689, 2006.

Wang, T., Wei, X. L., Ding, A. J., Poon, C. N., Lam, K. S., Li, Y. S., Chan, L. Y., and Anson, M.: Increasing surface ozone concentrations in the background atmosphere of Southern China, 1994–2007, Atmos. Chem. Phys., 9, 6217–6227, 2009.

Wang, X., Shen, Z., Cao, J., Zhang, L., Liu, L., Li, J., Liu, L., and Sun, Y.: Characteristics of surface ozone at an urban site of Xi'an in Northwest China, J. Environ. Monit., 14, 116–125, 2012.

Wang, Y., Zhang, Q., Jiang, J., Zhou, W., Wang, B., He, K., Duan, F., Zhang, Q., Philip, S. and Xie, Y.: Enhanced sulfate formation during China's severe winter haze episode in January 2013 missing from current models, J. Geophys. Res., 119(17), 10,425–10,440, doi:10.1002/2013JD021426, 2014.

Xu, J., Ma, J. Z., Zhang, X. L., Xu, X. B., Xu, X. F., Lin, W. L., Wang, Y., Meng, W., and Ma, Z. Q.: Measurement of ozone and its precursors in Beijing during summertime: impact of urban plumes on ozone pollution in downwind rural areas, Atmos. Chem. Phys., 11, 12241–12252, 2011.

Xue, L. K., Wang, T., Gao, J., Ding, A. J., Zhou, X. H., Blake, D. R., Wang, X. F., Saunders, S. M., Fan, S. J., Zuo, H. C., Zhang, Q. Z. and Wang, W. X.: Ground-level ozone in four Chinese cities: precursors, regional transport and heterogeneous processes, Atmos. Chem. Phys., 14(23), 13175–13188, doi:10.5194/acp-14-13175-2014, 2014.

Zhao, J., Levitt, N. P., Zhang, R. Y., and Chen, J. M.: Heterogeneous reactions of methylglyoxal in acidic media: implications for secondary organic aerosol formation, Environ. Sci. Technol., 40, 7682–7687, 2006.

Zhang, Q., Streets, D. G., Carmichael, G. R., He, K. B., Huo, H., Kannari, A., Klimont, Z., Park, I. S., Reddy, S., Fu, J. S., Chen, D., Duan, L., Lei, Y., Wang, L. T., and Yao, Z. L.: Asian emissions in 2006 for the NASA INTEX-B mission, Atmos. Chem. Phys., 9, 5131–5153, 2009.

Zhang, Y. H., Su, H., Zhong, L. J., Cheng, Y. F., Zeng, L. M., Wang, X. S., Xiang, Y. R., Wang, J. L., Gao, D. F., and Shao, M.: Regional ozone pollution and observation-based approach for analyzing ozone–precursor relationship during the PRIDE-PRD2004 campaign, Atmos. Environ., 42(25), 6203–6218, 2008.

753 Zhou, J., Ito, K., Lall, R., Lippmann, M., and Thurston, G.: Time-series analysis of mortality
754 effects of fine particulate matter components in Detroit and Seattle, Environ. Health
755 Persp., 119, 461–466, 2011.
756

Figure Captions

Figure 1. Map showing (a) the location of Xi'an in China, (b) WRF-CHEM model simulation domain with topography and (c) geographic distributions of surface monitoring stations. In (c), the blue squares represent the chemical species monitoring stations and the red circle is the IEECAS site. The red numbers denote meteorological observation sites. 1: Xi'an; 2: Xianyang; 3: Jinghe; 4: Lintong; 5: Chang'an; 6: Lantian. In addition, the area surrounded by the white rectangle in (c) is defined as Xi'an and surrounding areas according to the plume movement, and the area surrounded by the black line is the urban region of Xi'an.

Figure 2. Geographic distributions of anthropogenic emissions of (a) nitrogen oxide, (b) volatile organic compounds, and (c) biogenic isoprene emission in the simulation domain. The black lines present provincial boundaries in China.

Figure 3. Monthly minimum, 5th percentile, median, 95th percentile, and maximum of near-surface O_3 concentrations in the afternoon averaged over 13 observational sites in Xi'an from April 2013 to March 2014

Figure 4. Temporal variations of the observed surface (a) temperature, (b) relative humidity, (c) wind speed and (d) wind direction at Xianyang Meteorological Station, and near-surface (e) O_3 and (f) $PM_{2.5}$ concentrations averaged over 13 sites in Xi'an during summer of 2013. Red curves depict the simulation period (22-24 August) in this study.

Figure 5. Observed (black dots) and simulated (blue lines) diurnal profiles of (a) surface temperature and (b) relative humidity averaged over six meteorological sites from August 22 to 24, 2013.

Figure 6. Observed (black dots) and simulated (blue lines) diurnal profiles of surface wind speeds at six meteorological sites from August 22 to 24, 2013.

Figure 7. Same as Figure 6, but for surface wind directions

Figure 8. Pattern comparison of simulated vs. observed near-surface O_3 concentrations at 08:00 and 15:00 BJT from August 22 to 24, 2013. Colored squares: O_3 observations; color contour: O_3 simulations; black arrows: simulated surface winds.

Figure 9. Pattern comparison of simulated vs. observed near-surface NO_2 concentrations at 08:00 and 15:00 BJT from August 22 to 24, 2013. Colored squares: NO_2 observations; color contour: NO_2 simulations; black arrows: simulated surface winds.

Figure 10. Comparison of measured (black dots) and simulated (blue line) diurnal profiles of near-surface hourly (a) O_3 and (b) NO_2 averaged over all ambient monitoring stations from August 22 to 24, 2013.

Figure 11. (a) scatter plot of measured daily aerosol constituents with simulations and comparison of (b) measured and (c) modeled $PM_{2.5}$ chemical composition (%).

Figure 12. Pattern comparison of simulated vs. observed near-surface $PM_{2.5}$ concentrations at 08:00 and 15:00 BJT from August 22 to 24, 2013. Colored squares: $PM_{2.5}$ observations; color contour: $PM_{2.5}$ simulations; black arrows: simulated surface winds.

Figure 13. Comparison of measured (black dots) and simulated (blue line) diurnal profiles of near-surface hourly $PM_{2.5}$ averaged over all ambient monitoring stations from August 22 to 24, 2013.

Figure 14. Retrieved (black dots) and calculated (blue lines) diurnal profiles of (a) AOD and (b) aerosol SSA at 440 nm at IEECAS site from August 22 to 24, 2013, and pattern comparison of calculated vs. retrieved AOD at 550 nm at 10:00 BJT (c) on August 22 and (d) 23, 2013. Colored squares: retrieved AOD; color contour: calculated AOD.

Figure 15. Diurnal variations of the change in (a) $J[NO_2]$ and (b) O_3 concentrations averaged in Xi'an and surrounding areas due to aerosol effects from August 22 to 24, 2013.

Figure 16. Diurnal profiles of (a) O_3 concentrations and (b) O_3 changes averaged in Xi'an and surrounding areas caused by a 50% reduction of anthropogenic NO_x and VOCs emissions, respectively, from August 22 to 24, 2013. Blue line: the reference simulation; red line: the simulation with a 50% reduction of anthropogenic NO_x emissions; green line: the simulation with a 50% reduction of anthropogenic VOCs emissions.

Figure 17. Change in O_3 concentrations in the bottom model layer, averaged during O_3 peak time from August 22 to 24, 2013 due to a 50% reduction of anthropogenic (a) NO_x and (b) VOCs emissions, and the 3-day average ratio of $P(H_2O_2)/P(HNO_3)$ during O_3 peak time.

Figure 18. Diurnal variations of contributions of biogenic emissions to near-surface isoprene and O_3 concentrations averaged in Xi'an and surrounding areas from August 22 to 24, 2013.

Figure 19. Diurnal profiles of (a) O_3 concentrations and (b) O_3 contribution from various anthropogenic sources averaged in Xi'an and surrounding areas from August 22 to 24, 2013. Blue line: the reference simulation; brown line: the simulation without industry emissions; green line: the simulation without residential emissions; red line: the simulation without transportation emissions.

Figure 20. Diurnal profiles of (a) O_3 concentrations and (b) O_3 changes averaged in Xi'an and surrounding areas caused by a 50% reduction of various anthropogenic sources from August 22 to 24, 2013. Blue line: the reference simulation; brown line: the simulation with a 50% reduction of industry emissions; green line: the simulation with a 50% reduction of residential emissions; red line: the simulation with a 50% reduction of transportation emissions; the black line: the simulation with a 50% of all anthropogenic emissions.

838 Table 1 Air quality standards, individual air quality indices (IAQI) and their corresponding
839 hourly O_3 and $PM_{2.5}$ concentration limits
840

Air quality standards	IAQI	Hourly O_3 concentration ($\mu g\ m^{-3}$)	Hourly $PM_{2.5}$ concentration ($\mu g\ m^{-3}$)
Excellent	50	160	35
Good	100	200	75
Lightly polluted	150	300	115
Moderately polluted	200	400	150
Heavily polluted	300	800	250
Severely polluted	300+	800+	250+

841
842
843
844

Table 2 Summertime O_3 and $PM_{2.5}$ concentrations (averaged in the afternoon) in the main cities of Guanzhong basin, BTH, YRD, and PRD in China during 2013.

Region	City	O_3 (μg m^{-3})	$PM_{2.5}$ (μg m^{-3})
Guanzhong	Xi'an	104.6	48.5
BTH	Beijing	133.9	74.7
	Tianjin	116.9	78.1
	Shijiazhuang	140.4	86.6
YRD	Shanghai	122.9	47.1
	Hangzhou	110.5	35.0
	Nanjing	96.6	41.2
PRD	Guangzhou	94.9	29.4

852 Table 3 Statistical comparison of simulated and measured O_3, NO_2, $PM_{2.5}$, temperature,
853 relative humidity, and wind speed at monitoring sites from August 22 to 24, 2013.
854

Predictands	**Classification**	***MB***	***RMSE***	***IOA***
O_3 (μg m^{-3})	Averaged	-9.0	29.	0.91
NO_2 (μg m^{-3})	Averaged	-5.2	11.	0.73
$PM_{2.5}$ (μg m^{-3})	Averaged	-1.4	21.	0.92
Temperature (°C)	Averaged	-0.76	1.1	0.97
Relative Humidity (%)	Averaged	-4.5	5.5	0.92
Wind Speed (m s^{-1})	Xi'an	1.7	2.1	0.26
	Xianyang	1.3	1.5	0.61
	Jinghe	0.14	1.1	0.74
	Lintong	1.2	1.5	0.63
	Chang'an	0.69	1.2	0.47
	Lantian	0.43	1.1	0.61

855
856
857
858

Table 4 Occurrence days of the defined $PM_{2.5}$ and O_3 exceedance levels during 2013 summertime

	Beijing	Tianjin	Shijiazhuang	Ji'nan	Taiyuan	Xi'an
[1]Level I	57	65	64	72	53	61
[2]Level II	33	41	43	41	28	20

[1]hourly $PM_{2.5}$ and O_3 concentrations exceeding 35 and 160 μg m^{-3}, respectively
[2]hourly $PM_{2.5}$ and O_3 concentrations exceeding 75 and 200 μg m^{-3}, respectively
The original data are from China MEP.

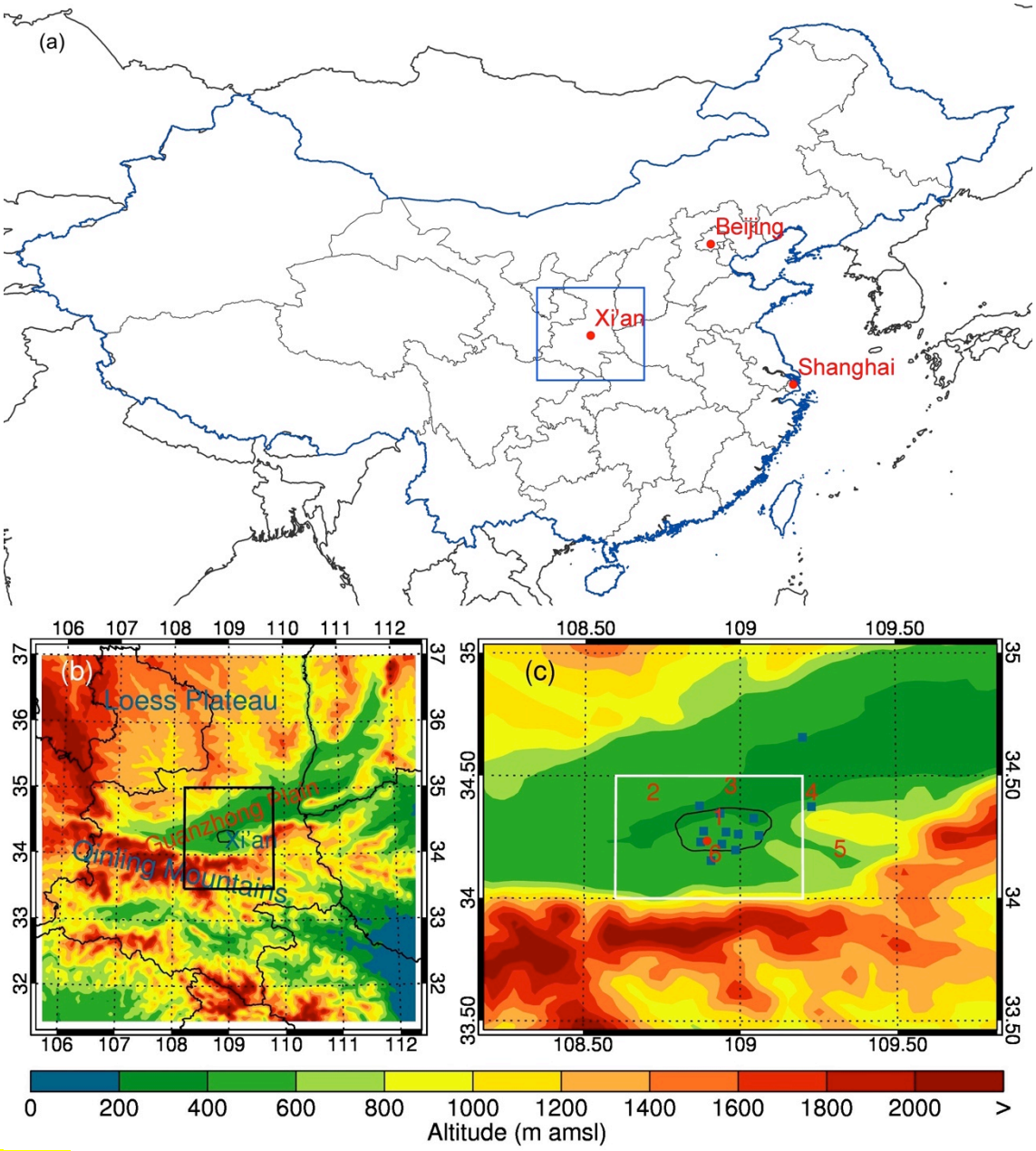
(a)
Beijing
Xi'an
Shanghai
(b)
Loess Plateau
Guanzhong Plain
Xi'an
Qinling Mountains
(c)
1
2
3
4
5
106 107 108 109 110 111 112
32 33 34 35 36 37
108.50 109 109.50
33.50 34 34.50 35
0 200 400 600 800 1000 1200 1400 1600 1800 2000 >
Altitude (m amsl)

Figure 1

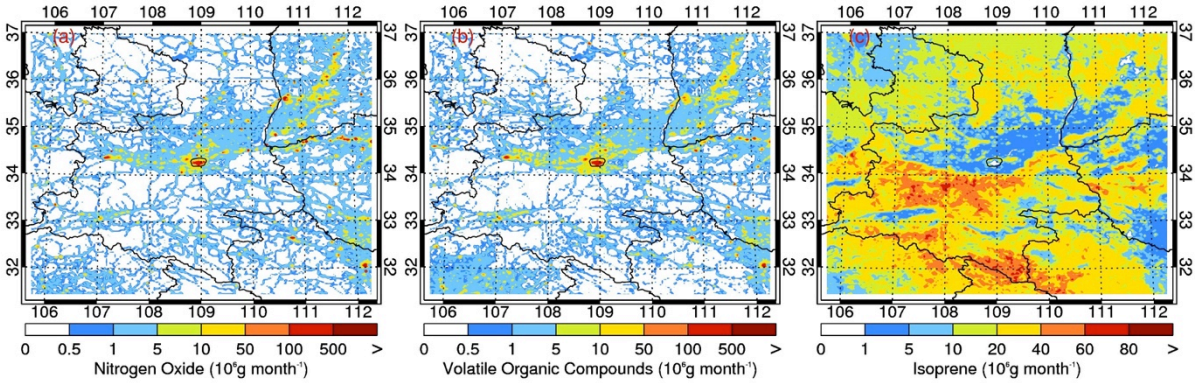
(a)
(b)
(c)
106 107 108 109 110 111 112
32 33 34 35 36 37
0 0.5 1 5 10 50 100 500 >
Nitrogen Oxide (10⁶g month⁻¹)
0 0.5 1 5 10 50 100 500 >
Volatile Organic Compounds (10⁶g month⁻¹)
0 1 5 10 20 40 60 80 >
Isoprene (10⁶g month⁻¹)

Figure 2

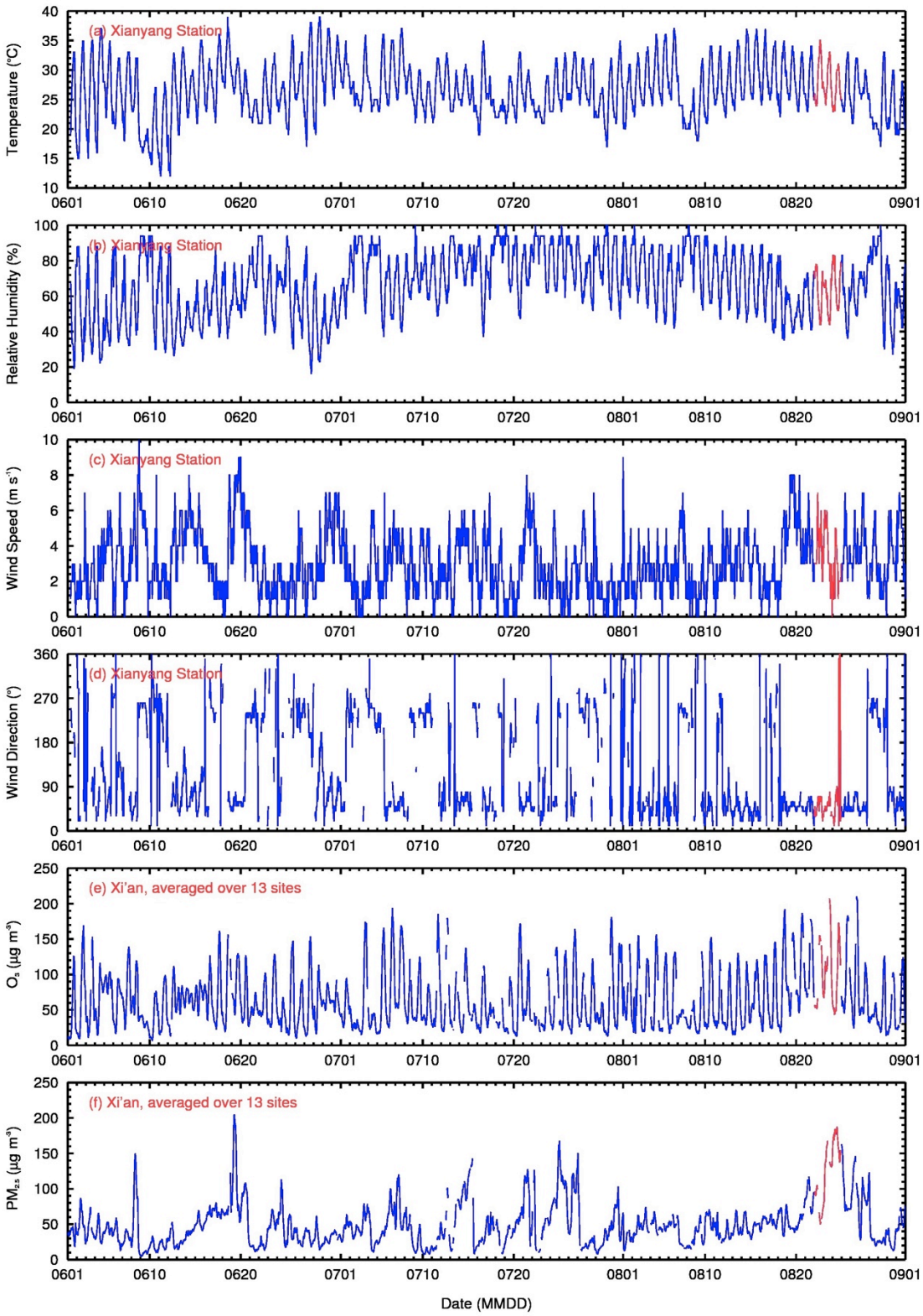
(a) Xianyang Station
Temperature (°C)
(b) Xianyang Station
Relative Humidity (%)
(c) Xianyang Station
Wind Speed (m s⁻¹)
(d) Xianyang Station
Wind Direction (°)
(e) Xi'an, averaged over 13 sites
O₃ (μg m⁻³)
(f) Xi'an, averaged over 13 sites
PM₂.₅ (μg m⁻³)
0601
0610
0620
0701
0710
0720
0801
0810
0820
0901
Date (MMDD)

Figure 3

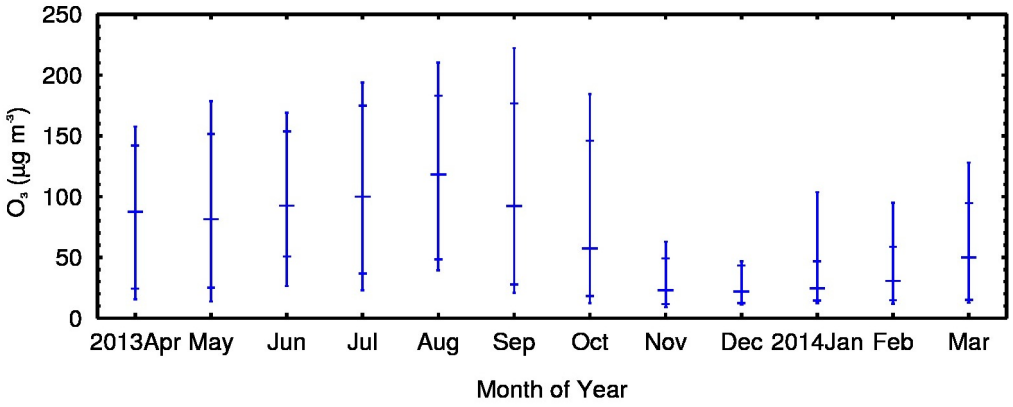
250
200
150
100
50
0
O_3 (µg m^{-3})
2013Apr May Jun Jul Aug Sep Oct Nov Dec 2014Jan Feb Mar
Month of Year

Figure 4

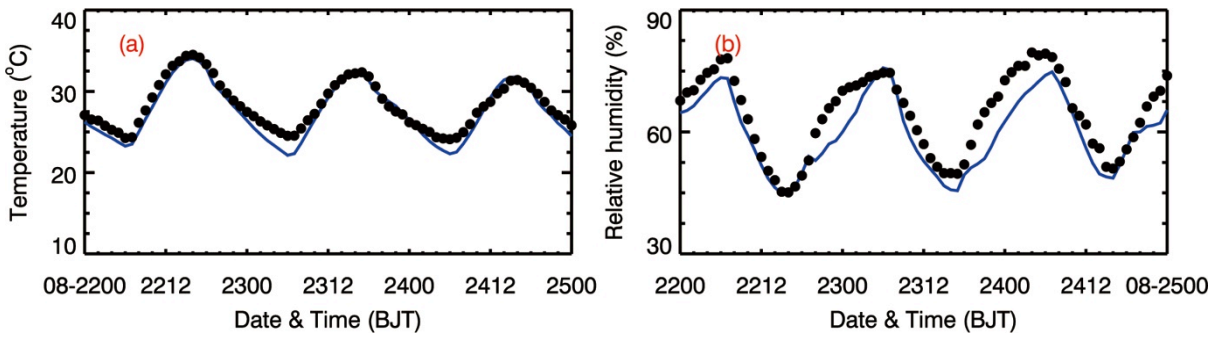
(a)
Temperature (°C)
40
30
20
10
08-2200
2212
2300
2312
2400
2412
2500
Date & Time (BJT)
(b)
Relative humidity (%)
90
60
30
2200
2212
2300
2312
2400
2412
08-2500
Date & Time (BJT)

Figure 5

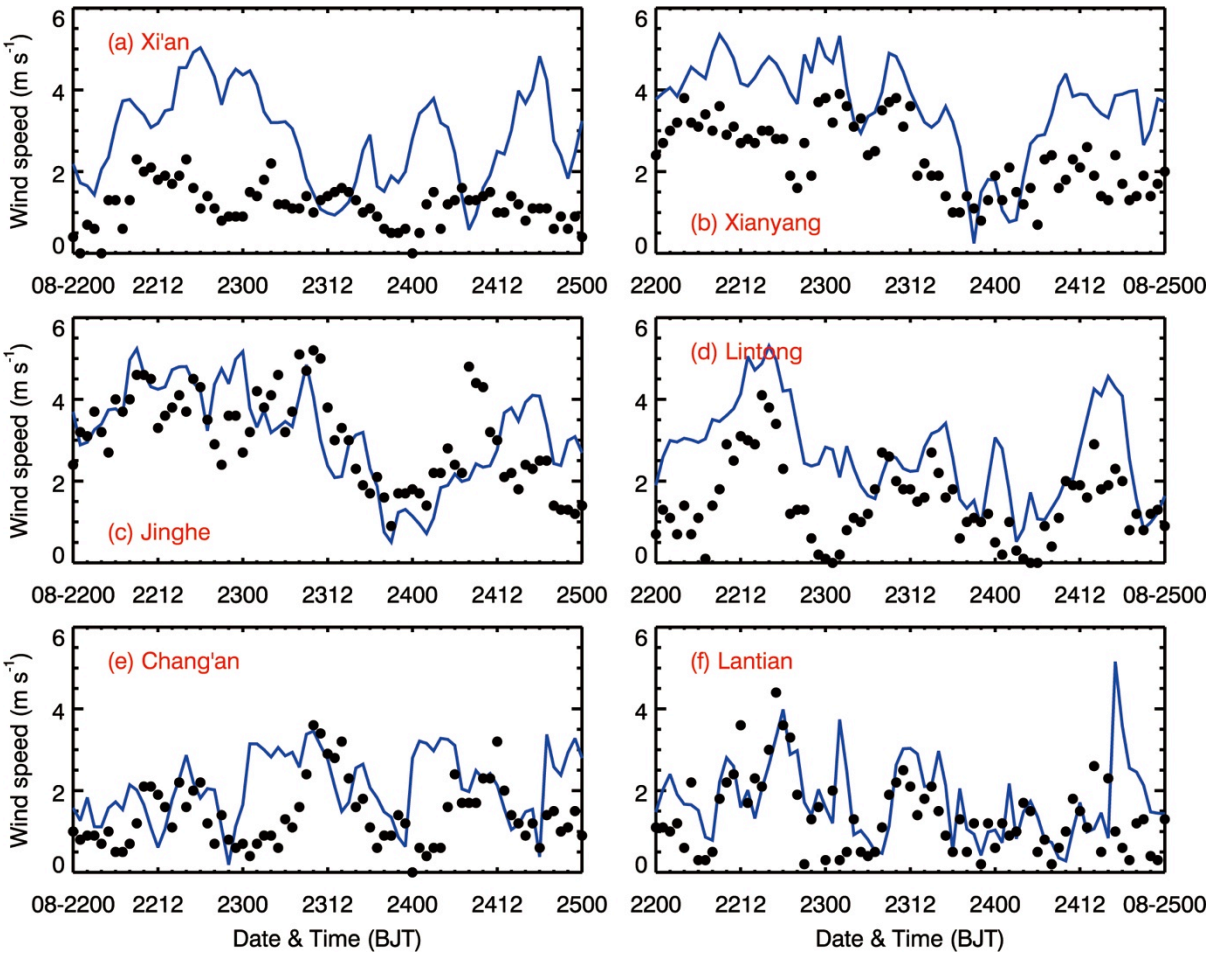
(a) Xi'an
(b) Xianyang
(c) Jinghe
(d) Lintong
(e) Chang'an
(f) Lantian
Wind speed (m s-1)
0
2
4
6
08-2200
2212
2300
2312
2400
2412
2500
08-2500
Date & Time (BJT)

Figure 6

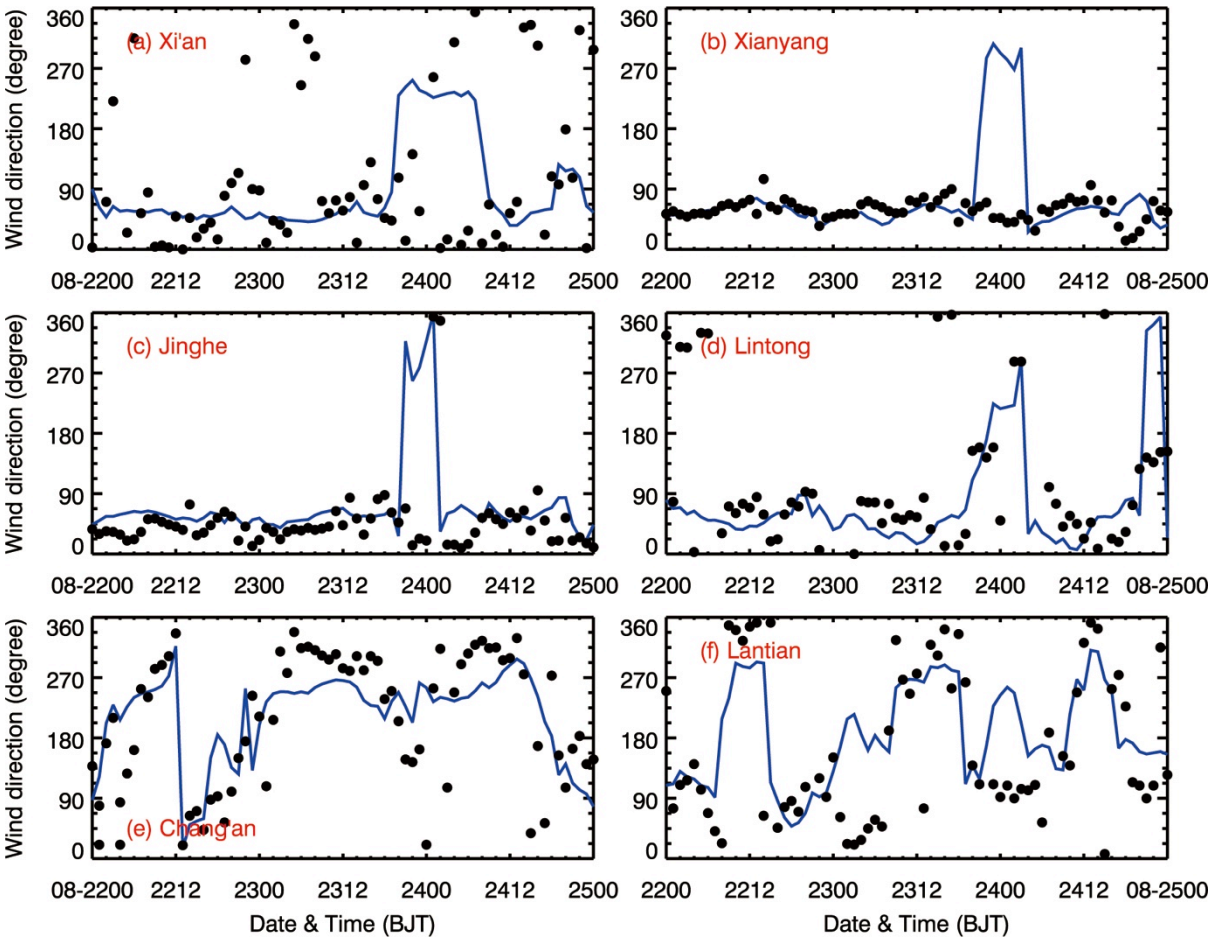
(a) Xi'an
(b) Xianyang
(c) Jinghe
(d) Lintong
(e) Changan
(f) Lantian
Wind direction (degree)
0
90
180
270
360
08-2200
2212
2300
2312
2400
2412
2500
2200
08-2500
Date & Time (BJT)

Figure 7

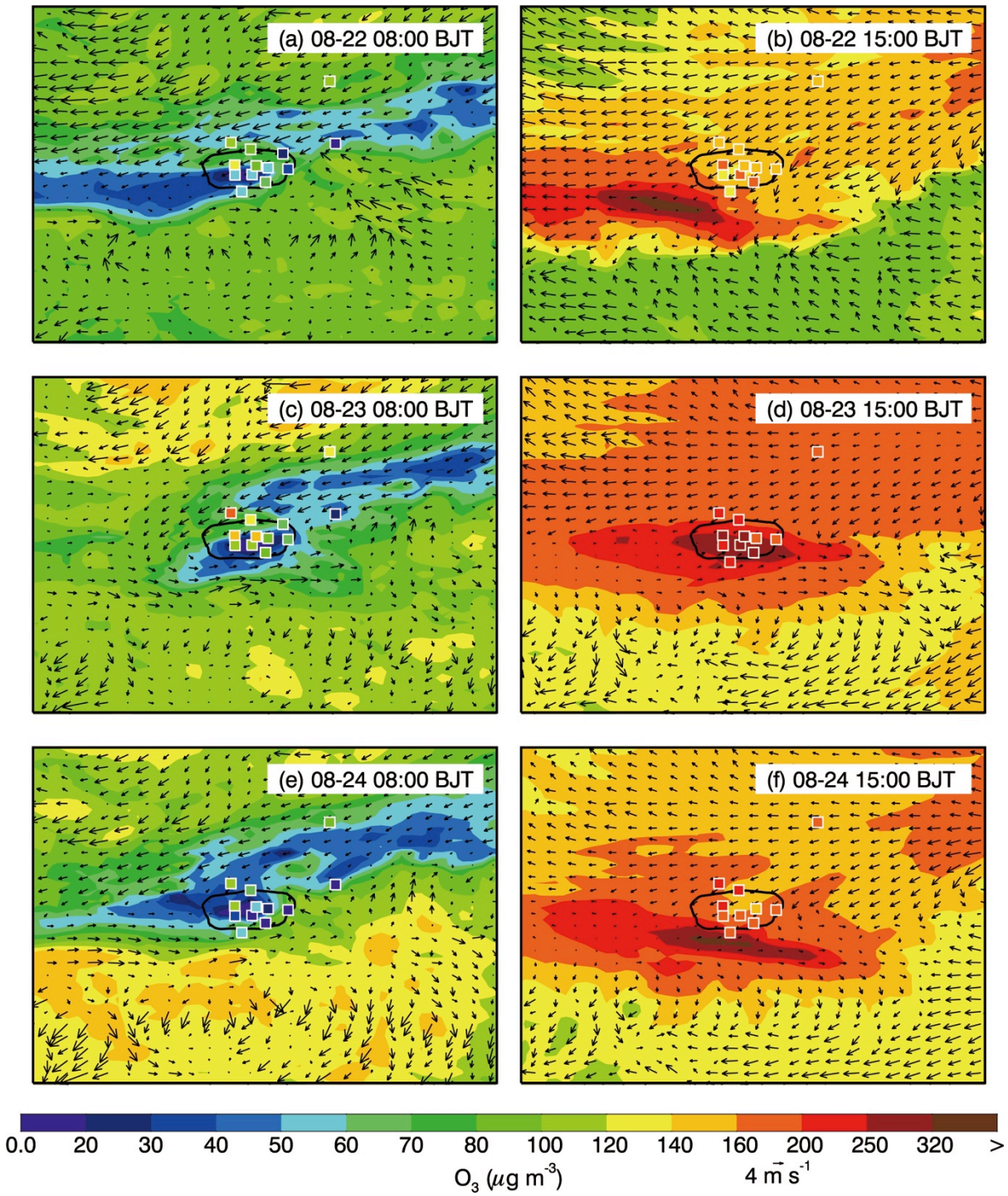
(a) 08-22 08:00 BJT
(b) 08-22 15:00 BJT
(c) 08-23 08:00 BJT
(d) 08-23 15:00 BJT
(e) 08-24 08:00 BJT
(f) 08-24 15:00 BJT
0.0 20 30 40 50 60 70 80 100 120 140 160 200 250 320 >
O3 (μg m-3)
4 m s-1

Figure 8

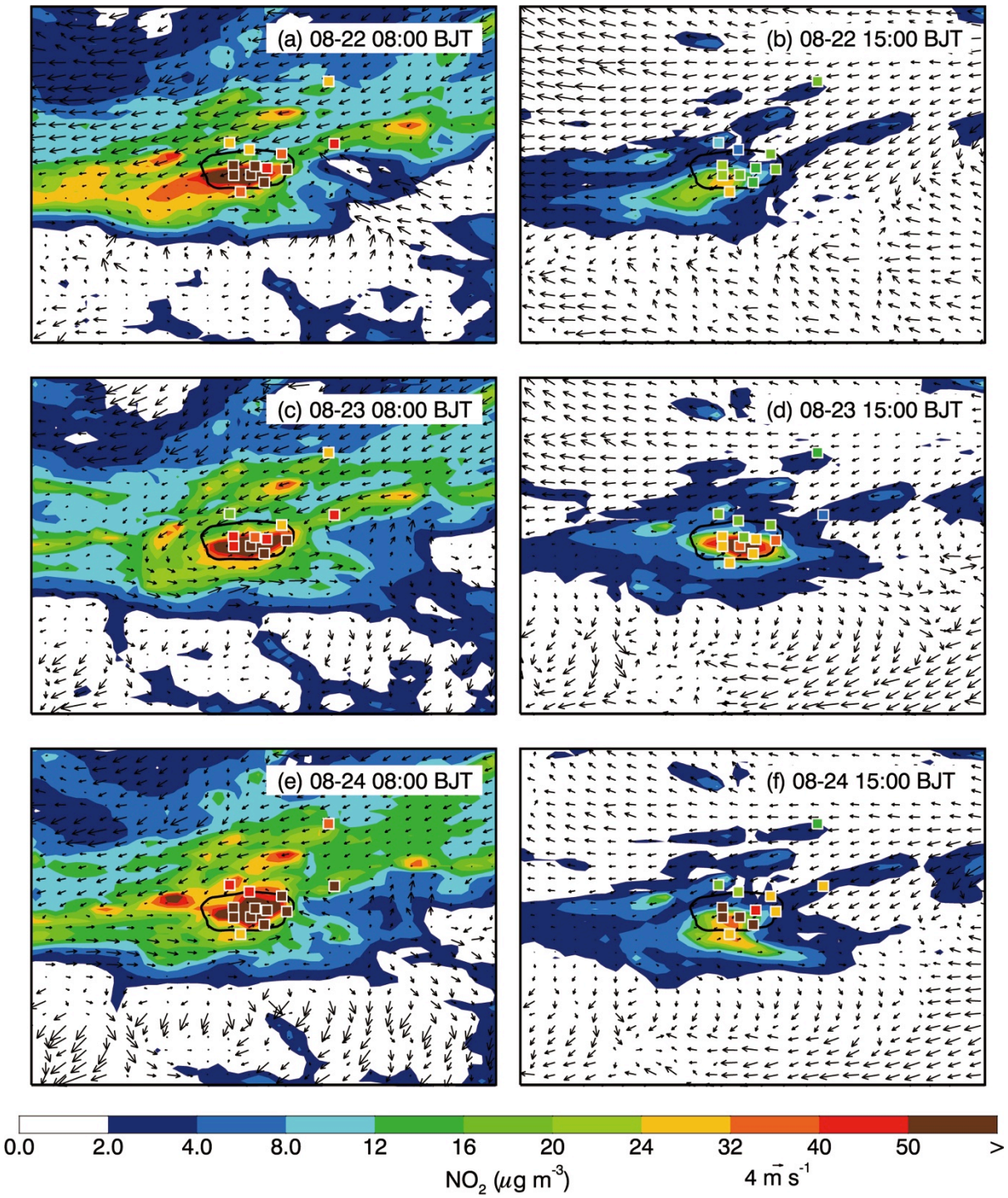
(a) 08-22 08:00 BJT
(b) 08-22 15:00 BJT
(c) 08-23 08:00 BJT
(d) 08-23 15:00 BJT
(e) 08-24 08:00 BJT
(f) 08-24 15:00 BJT
0.0
2.0
4.0
8.0
12
16
20
24
32
40
50
>
NO2 (μg m-3)
4 m s-1

Figure 9

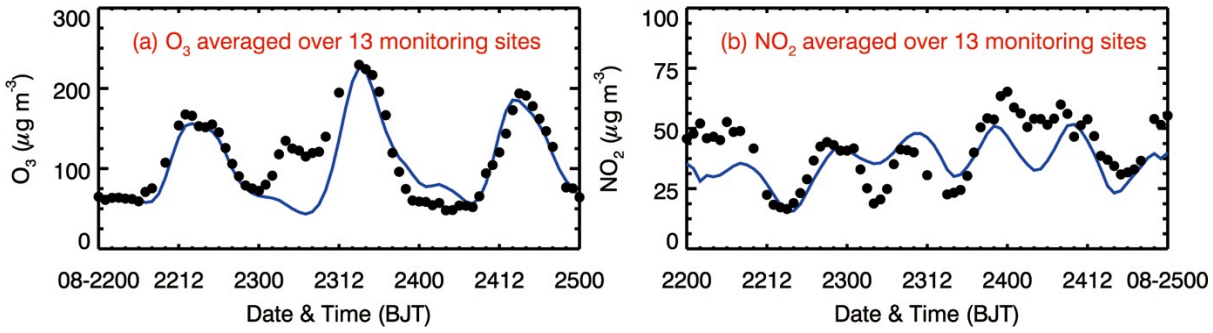
(a) O_3 averaged over 13 monitoring sites
O_3 (μg m^{-3})
300
200
100
0
08-2200
2212
2300
2312
2400
2412
2500
Date & Time (BJT)
(b) NO_2 averaged over 13 monitoring sites
NO_2 (μg m^{-3})
100
75
50
25
0
2200
2212
2300
2312
2400
2412
08-2500
Date & Time (BJT)

Figure 10

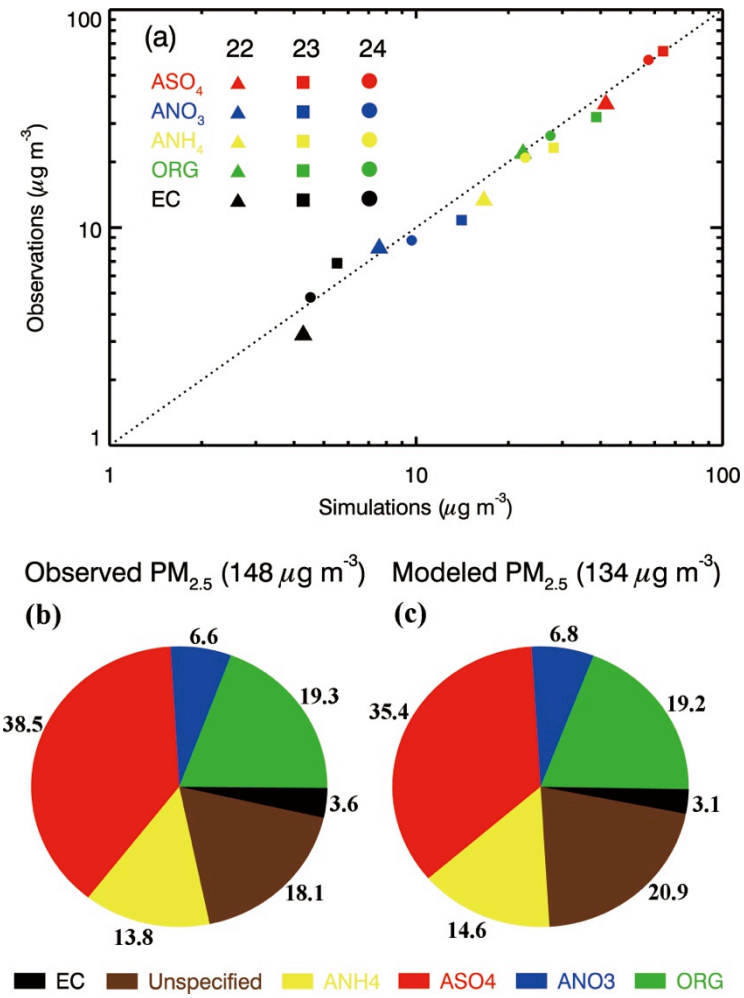
(a)
22
23
24
ASO4
ANO3
ANH4
ORG
EC
Observations (μg m-3)
Simulations (μg m-3)
100
10
1
Observed PM2.5 (148 μg m-3)
Modeled PM2.5 (134 μg m-3)
(b)
(c)
6.6
19.3
38.5
3.6
18.1
13.8
6.8
19.2
35.4
3.1
20.9
14.6
EC
Unspecified
ANH4
ASO4
ANO3
ORG

Figure 11

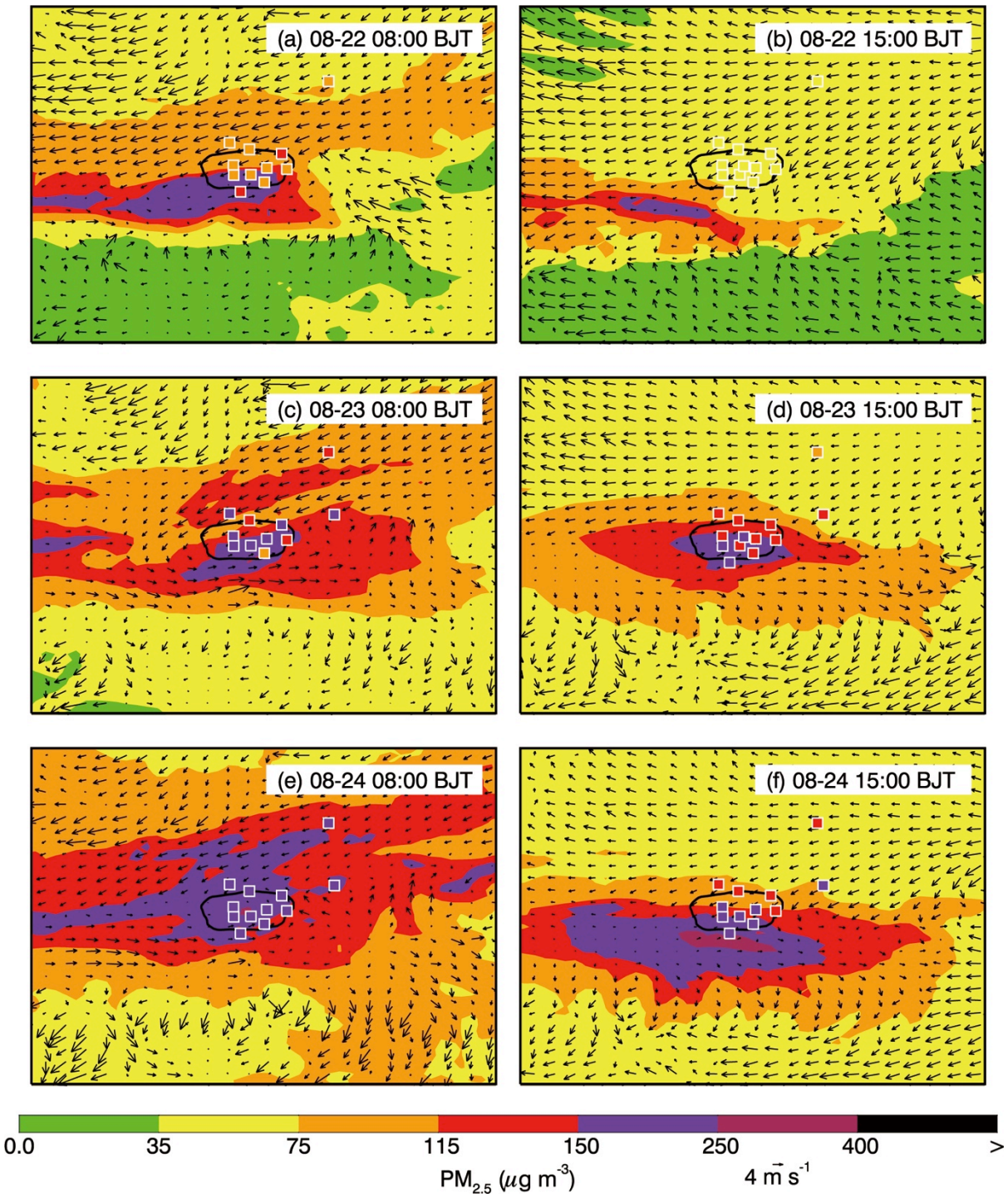
(a) 08-22 08:00 BJT
(b) 08-22 15:00 BJT
(c) 08-23 08:00 BJT
(d) 08-23 15:00 BJT
(e) 08-24 08:00 BJT
(f) 08-24 15:00 BJT
0.0
35
75
115
150
250
400
>
PM2.5 (μg m-3)
4 m s-1

Figure 12

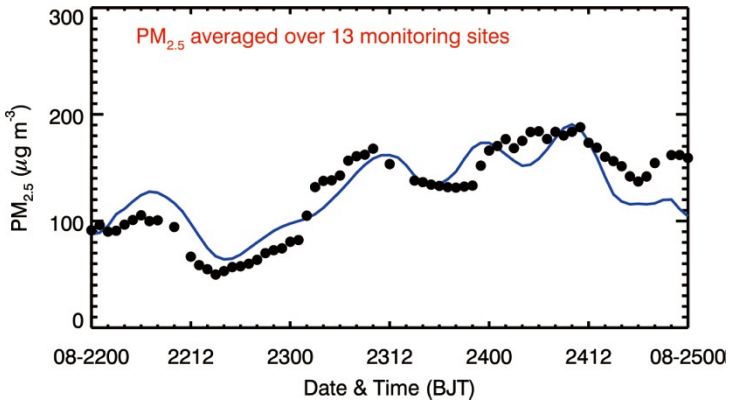
PM2.5 averaged over 13 monitoring sites
PM2.5 (μg m-3)
300
200
100
0
08-2200
2212
2300
2312
2400
2412
08-2500
Date & Time (BJT)

Figure 13

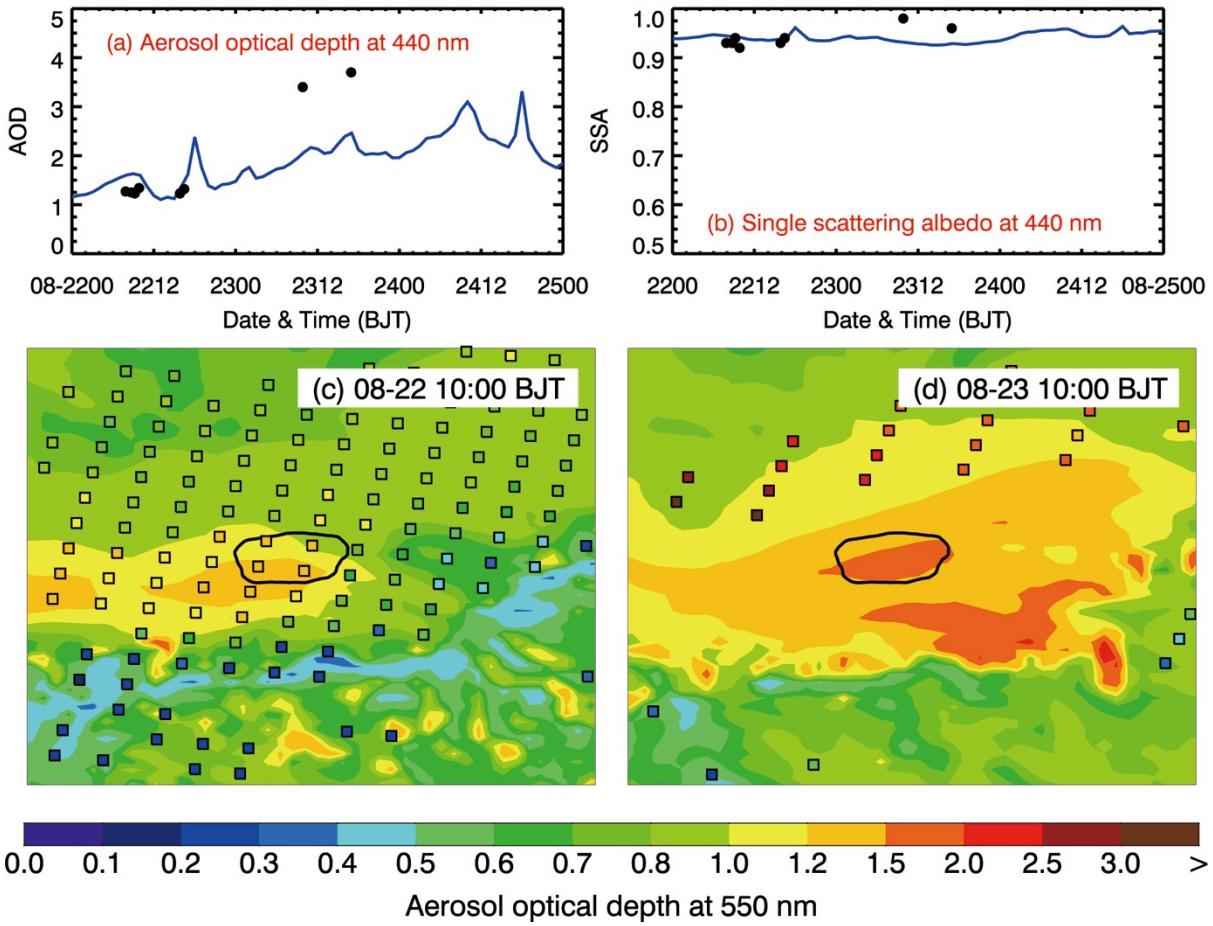
(a) Aerosol optical depth at 440 nm
AOD
0
1
2
3
4
5
08-2200
2212
2300
2312
2400
2412
2500
Date & Time (BJT)
(b) Single scattering albedo at 440 nm
SSA
0.5
0.6
0.7
0.8
0.9
1.0
2200
2212
2300
2312
2400
2412
08-2500
Date & Time (BJT)
(c) 08-22 10:00 BJT
(d) 08-23 10:00 BJT
0.0
0.1
0.2
0.3
0.4
0.5
0.6
0.7
0.8
1.0
1.2
1.5
2.0
2.5
3.0
>
Aerosol optical depth at 550 nm

Figure 14

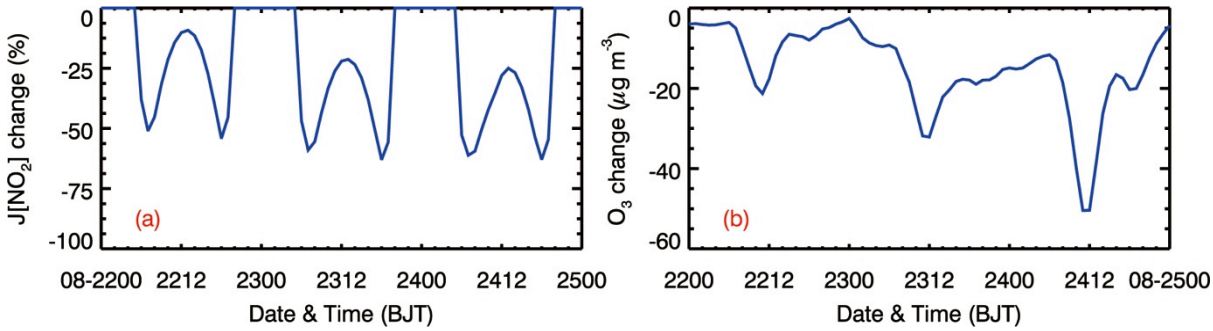
J[NO2] change (%)
0
-25
-50
-75
-100
(a)
08-2200
2212
2300
2312
2400
2412
2500
Date & Time (BJT)
O3 change (μg m-3)
0
-20
-40
-60
(b)
2200
2212
2300
2312
2400
2412
08-2500
Date & Time (BJT)

Figure 15

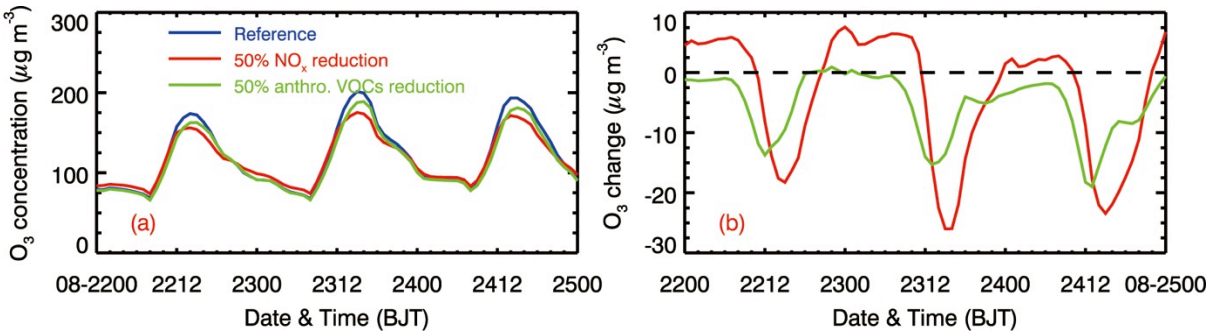
Reference
50% NOx reduction
50% anthro. VOCs reduction
O3 concentration (μg m-3)
300
200
100
0
(a)
08-2200
2212
2300
2312
2400
2412
2500
Date & Time (BJT)
O3 change (μg m-3)
10
0
-10
-20
-30
(b)
2200
2212
2300
2312
2400
2412
08-2500
Date & Time (BJT)

Figure 16

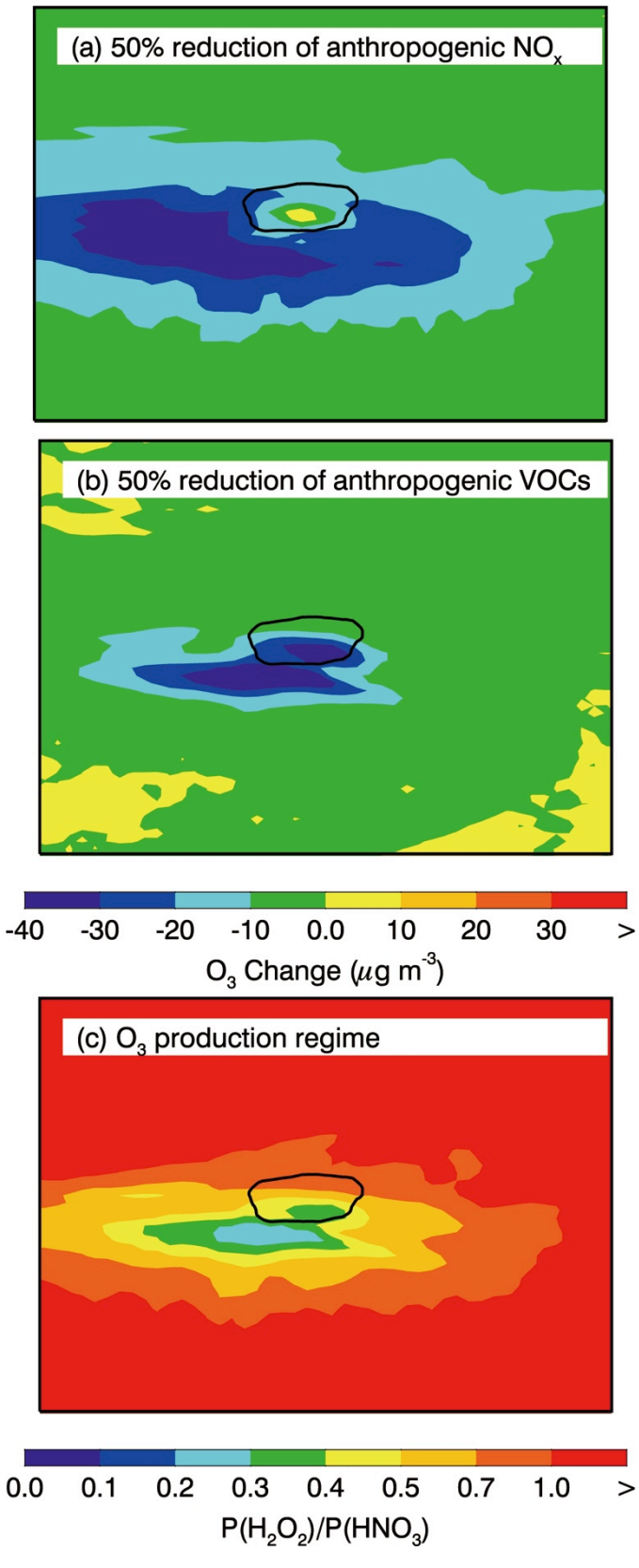

977
978
979 Figure 17
980
981
982
983

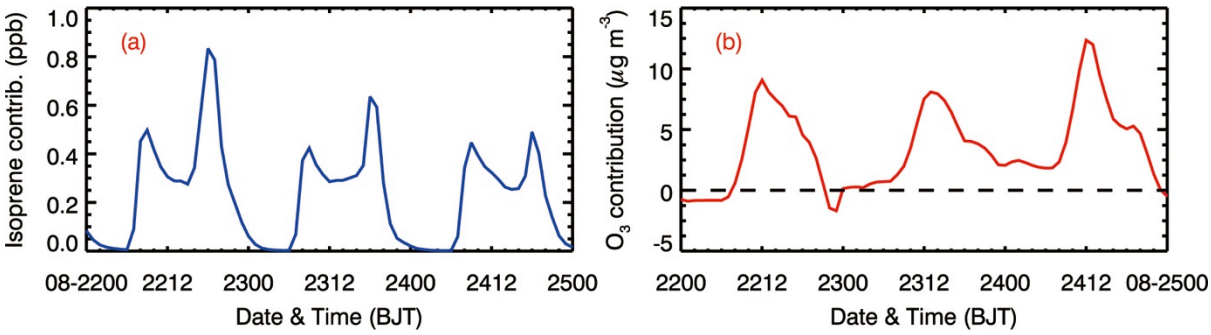
(a)
Isoprene contrib. (ppb)
1.0
0.8
0.6
0.4
0.2
0.0
08-2200
2212
2300
2312
2400
2412
2500
Date & Time (BJT)
(b)
O3 contribution (μg m-3)
15
10
5
0
-5
2200
2212
2300
2312
2400
2412
08-2500
Date & Time (BJT)

Figure 18

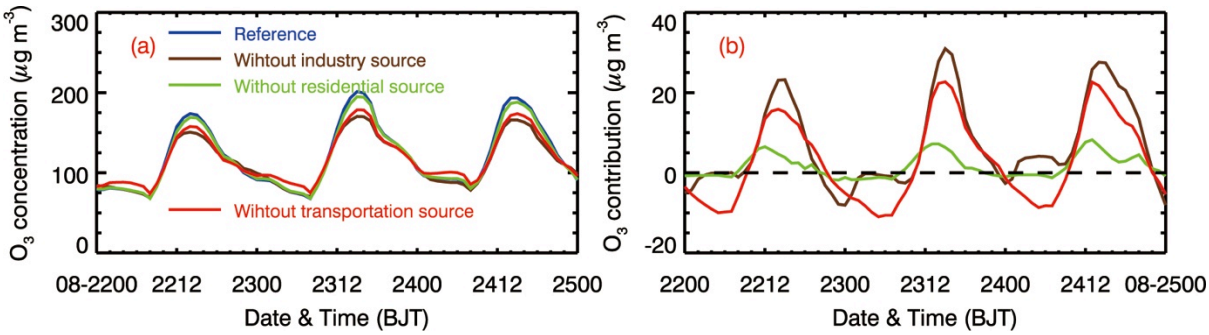
(a)
Reference
Wihtout industry source
Without residential source
Wihtout transportation source
O3 concentration (μg m-3)
300
200
100
0
08-2200
2212
2300
2312
2400
2412
2500
Date & Time (BJT)
(b)
O3 contribution (μg m-3)
40
20
0
-20
2200
2212
2300
2312
2400
2412
08-2500
Date & Time (BJT)

Figure 19

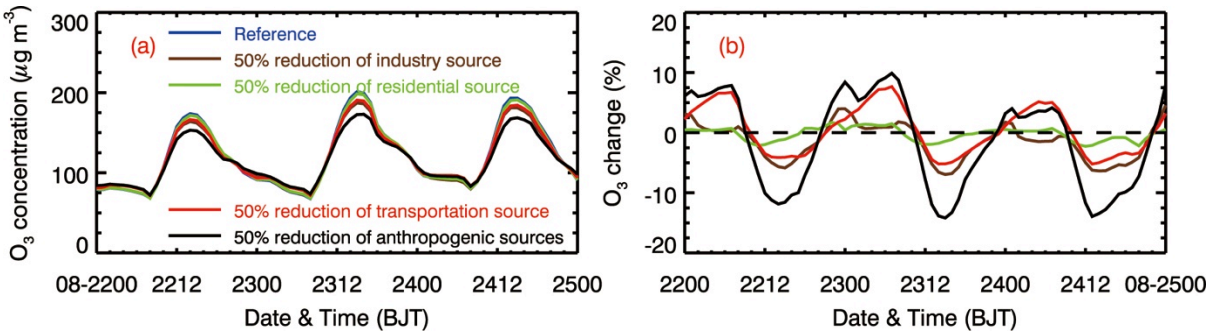
(a)
Reference
50% reduction of industry source
50% reduction of residential source
50% reduction of transportation source
50% reduction of anthropogenic sources
O3 concentration (μg m-3)
300
200
100
0
08-2200
2212
2300
2312
2400
2412
2500
Date & Time (BJT)
(b)
O3 change (%)
20
10
0
-10
-20
2200
2212
2300
2312
2400
2412
08-2500
Date & Time (BJT)

Figure 20